The Classical Lattice-Gas Method

Jeffrey Yepez
Jeffrey.Yepez@hanscom.af.mil
http://qubit.plh.af.mil

February 1999

Contents

1 Introduction **3**
1.1 Background . . . 3
1.2 Algorithmic Scheme . . . 4
1.3 History of Lattice-Gas Developments . . . 4
1.4 Lattice-Gas Applications to Multiphase Fluid Dynamics . . . 6
1.5 Limitations and Drawbacks of Classical Lattice Gases . . . 7
1.6 The Navier-Stokes Equation . . . 8
1.7 Dimensionless Numbers . . . 9

2 An Analytical Method for Predicting Macroscopic Behavior **11**
2.1 Mesoscopic Scale . . . 11
2.1.1 Derivation of the Linearized Kinetic Equation . . . 11
2.1.2 The Approach to Steady-State Equilibrium . . . 12
2.1.3 Linearized Lattice Boltzmann Equation . . . 13
2.1.4 Dispersion Relations . . . 14
2.1.5 Criterion for Deviations from Local Equilibria . . . 15
2.2 Macroscopic Scale . . . 16
2.2.1 Eigensystem of the Linearized Collision Operator . . . 16
2.2.2 Chapman-Enskog Expansion . . . 17
2.2.3 Derivation of the Continuum Equations . . . 19

3 A One-Dimensional Model with Conserved Mass and Momentum **23**
3.1 Microscopic Rules . . . 23
3.2 Model Analysis . . . 24
3.3 Comparing Analytical and Numerical Predictions . . . 29

4 A Two-Dimensional Model with Conserved Mass and Momentum **33**
4.1 Microscopic Rules . . . 33
4.2 Model Analysis . . . 35
4.3 Comparing Analytical and Numerical Predictions . . . 41
4.3.1 Single-Particle Probability of Occupancy in the Subsonic Limit . . . 41
4.3.2 Measuring the Shear Viscosity Using the Decay of a Sinusoidal Shear Wave . 42
4.3.3 Measuring the Bulk Viscosity Using the Decay of a Sinusoidal Compressional Wave . . . 45

5 Conclusion **49**

A Small Mach Number Expansion of the Occupancy Probability **51**

Chapter 1

Introduction

Presented is a review of the *classical lattice-gas method* that deals with an artificial many-body system of particles that has severely discretized microscopic dynamics and that behaves like a viscous Navier-Stokes fluid in the long wavelength hydrodynamic limit. We explain and analytically quantify how the artificial lattice-gas system behaves and we derive a set of criterion that specifies under what conditions it can serve as an appropriate model of a viscous and compressible fluid. Then, we show how the lattice-gas algorithm works using two test models. Finally, we compare the numerical predictions obtained from a variety of different simulations of these two test models to the respective analytical predictions we previously obtained for these models. The resulting numerical and analytical predictions are in good agreement in all cases, but this is only after many failed attempts that were incrementally corrected over time by removing flaws from the derivation of the analytical predictions as well as removing numerical bugs in the implementation of the algorithm and data collection methodology. Therefore, the reason for the consistently good agreement between numerical and analytical predictions is that the derived criteria set has been so sharply delineated that we now know with great accuracy how to initialize the numerical model within a narrow parameter regime where the lattice-gas system is operative. If the initial state of the lattice-gas system is outside this narrow operating regime, the numerical predictions are not at all in agreement with the analytical predictions and the behavior of the long wavelength modes in the system can no longer be classified as hydrodynamical. We have not attempted to catalog any of the non-hydrodynamical behaviors of a classical lattice-gas system. Instead, we have chosen to pursue a narrower goal, which as it turns out is computationally more difficult to pursue, where we run the algorithm only in a parameter regime where it behaves like a fluid.

1.1 Background

Much information about the details of the microscopic state of a many-body system is not relevant to the hydrodynamic behavior of the many-body system at the macroscopic scale. So in numerically simulating the macroscopic scale fluid behavior, it is possible to arrange for the computer to keep track of many fewer particles than are in the actual system. In a typical lattice-gas simulation of fluid, there are about 10^9 particles. In the simplest type of simulation, all the particles are indistinguishable and move independently of one another, except that groups of particles may collide together when they arrive at the same point. Over a decade ago, a classical lattice gas in two spatial dimensions was found to behave like a viscous Navier-Stokes fluid at the macroscopic scale by Wolfram [1] and by Frisch, Hasslacher, and Pomeau [2]. This is known as the *FHP lattice gas*. Soon after this discovery, a classical lattice gas was found to model three-dimensional fluids [3]. In the simulation, there may also be fixed obstacles with which the particles have perfectly elastic collisions. For example, one can simulate vortex shedding in a fluid flowing around a fixed object [4, 5, 6]. The value of shear viscosity for classical lattice-gas fluids has been studied by many researchers, including Wolfram [1], Frisch

et al. [3], Somers and Rem [7], Hénon [8]. In the case where there is an attractive force between particles spatially separated, multiphase fluid-like behavior is observed [9, 10, 11, 12, 13, 14, 15, 16] (this is a principal application of the lattice-gas method).

Microscopic classical lattice-gas models of Navier-Stokes fluids are now well understood. The lattice-gas method has been undergoing improvement, beginning in the mid 1970's up to the present day by many researchers, including Hardy, de Pazzis and Pomeau [17], Kadanoff, McNamara, and Zanetti [18, 19, 20, 21], Boghosian *et al.* [22, 23, 24, 25], Boon *et al.* [26, 27], Ernst, Das, Brito,*et al.* [28, 29, 30, 31], Hénon [8, 32], Doolen, S. Chen, *et al.* [33, 34, 35, 36, 37, 38], Frisch, Pomeau, d'Humières *et al.* [2, 3], Appert, Zeleski, and Rothman *et al.* [9, 10, 11, 12, 13], and Yepez [14, 15, 16, 39, 40]. This is by no means either an exhaustive list of all researchers or publications in this subject. An exhaustive preprint archive is maintained at Los Alamos National Laboratory (see "http://xyz.lanl.gov/archive/comp-gas").

1.2 Algorithmic Scheme

A lattice gas is a system of identical particles where the particles move on a discrete spatial lattice. The spatial lattice is an array of points (which is also referred to as *sites* or *nodes*), arranged in a regular crystallographic fashion, and the lattice appears exactly the same from whichever of the points the array is viewed. This kind of lattice is called a *Bravais lattice*. In the case of a *single-speed lattice gas*, as the name implies, all the particles in the system move at the same speed: $c = \frac{\ell}{\tau}$, where ℓ is the distance between two neighboring sites of the lattice and τ is the time it takes for a particle to hop from one site to another site in the nearest neighboring vicinity. In a lattice-gas system, all particles move at same time and then they collide. The propagation step is called the *streaming phase*. The propagation time, τ, for particle streaming is also the *update time* for the entire system because we imagine that the *collision phase* of the update procedure happens instantaneously and homogeneously across the entire system of particles. The smallest possible mean free path length for a particle in a lattice-gas fluid is on the order of the grain size of the lattice, ℓ. There exists a new and unique global arrangement of particles, referred to as a *state* of the system, following each and every update time period τ.[1]

The *local state* of each particle is specified by a position coordinate and a momentum vector. We can think of each local state of the system as having a unique position in the lattice and a unique orientation or *displacement vector* (corresponding to a momentum vector for particle's motion). As a particle moves through the spatial lattice, it hops from local state to local state. Each local state is like a container that can temporarily hold a particle that is moving in a particular direction.

In the simplest type of lattice-gas model, no more than one particle can occupy a single local state. However, more than one particle can reside at a single site at any one time since there are B number of local states per site. Each local state holds a particle at that site moving in a unique direction. Hence, the maximum number of particles that can coexist on a single site equals the number of nearest neighboring sites, since it is possible that particles can hop from all nearest neighboring sites to one particular site all at once. Of course, the minimum number of particles that can reside at a site is zero, which can happen when all the particles at that site move away and no new ones enter from any of the neighboring sites. So the information needed to encode a particle's occupancy of a local state is a single classical bit associated with that site and that local state. If the bit is *on*, a particle is there. If the bit is *off*, then no particle occupies that local state.

1.3 History of Lattice-Gas Developments

Let me briefly review some of the developments of the lattice-gas method applied to fluid dynamics simulation. An overview of the lattice gas fluids has been given by Boghosian [41]. Lattice

[1] The fact that every state of the system is unique follows from the principle of detailed-balance which is obeyed during the on-site collisions that may occur after multiple particles arrive at a single site.

gases are a special case of cellular automata, originally introduced by von Neumann and Ulam in 1948 [42] and popularized in the 1980's by Fredkin [43] and by Stephen Wolfram [44, 45]. A broad treatment of the cellular automata subject is presented by Toffoli and Margolus in their book on cellular automata machines [46]. Following the cellular automata paradigm, lattice gases are suited to fine-grained parallel processing, also called massively parallel processing.

A simple lattice-gas model of discrete molecular dynamics on a square lattice was analytically investigated in the early 1970's by the French, J. Hardy, O. de Pazzis, and Yves Pomeau [17]. Computer implementations were not carried out until a decade later. Their model, known as the HPP model, was the first classical lattice gas to reproduce hydrodynamic behavior at the macroscopic scale. In the late 1970's, cellular automata research was underway at the Information Mechanics Group at MIT on reversible computation by Fredkin, Toffoli, and Margolus [47, 43, 48]. They built fine-grained special-purpose machines to simulate physics-like models [49, 48]. A review of the kind of cellular automata modeling done in the early 1980's is given by Vichniac [50]. Stephen Wolfram, a visitor at the Information Mechanics Group in 1983, popularized cellular automata as simple models of self-organization amenable to statistical mechanics analysis [44, 51].

In 1985 Wolfram completed the first hydrodynamic lattice-gas simulations on a triangular lattice [52] on the first Connection Machine—at that time, lattice gases were a very appropriate application for the bit oriented single instruction, multiple data Connection Machine [53]. After visiting the MIT Information Mechanics Group and seeing a type of HPP lattice-gas running on the cellular automata machine CAM-5 of Toffoli and Margolus [54, 49], Pomeau was inspired by seeing hydrodynamic-like behavior (for example, the superposition of sound pulses) occurring at the macroscopic scale by simple rules homogeneously applied at the microscopic scale. By 1986 Frisch, Hasslacher, and Pomeau had reported the existence of an isotropic two-dimensional lattice gas on the triangular lattice [2] that is described by the Navier-Stokes equation (1.4). Their model is referred to as the FHP model. Accompanying the seminal 1986 FHP paper was a paper by Margolus, Toffoli, and Vichniac on cellular automata machines for fluid dynamics modeling [55]. The contribution of Margolus *et al.* was meant to complement the work of Frisch *et al.*, pointing out the benefit of dedicated computational hardware for lattice-gas models. In the same year Wolfram completed a detailed treatment of the basic theory of discrete lattice-gas fluids using symmetry considerations and worked out the mesoscopic scale description in the Boltzmann approximation [1].

By 1987 the lattice-gas methodology was extended to model three-dimensional flows by Frisch, d'Humières, Hasslacher, Lallemand, Pomeau and Rivet [3]. The minimal lattice found was the face centered hypercubic (FCHC) lattice. The FCHC lattice is four-dimensional with 24-nearest neighbors. It is projected onto three dimensions in a simple fashion by limiting the depth of the fourth dimension of the simulation volume to one lattice link. Much effort was spent on finding optimal collisions to minimize the viscosity of the fluid [8].[2]

It was realized in the late 1980's by Rivet and Frisch [56] and by McNamara and Zanetii [57] that a lattice gas could be simulated directly at the mesoscopic scale using the lattice Boltzmann equation. In place of the discrete microscopic representation, one begins at the mesoscopic scale by representing the probability of a particle occupying a local state. It has the advantage of eliminating inherent noisy fluctuations in the simulation, but at the expense of discarding the particle-particle correlations.

In 1954, D. Bhatnager, E. Gross, and M. Krook showed how the collision integral in the Boltzmann equation can be reduced to a simple diagonal form [58]; this is termed the *BGK approximation*. A cutoff to the collision integral is made by neglecting high order particle-particle correlations to cast the Boltzmann equation as an approximate partial differential equation. Using the BGK approximation of the collision intregal, Chen, S. Chen and Mattaeus showed how one could remove the anomalies (such as non-Galilean invariance) that occur at the macroscopic scale by tailoring the

[2] This task is difficult because the FCHC lattice gas has 2^{24} or 16.7 million local configurations. In practice, all possible collisions are not included in a simulation because of the large demand for local memory needed to pre-store all the necessary collisional events in table look-up format. To ease memory loads, Somers and Rem used lattice isometries to reduce the size of look-up tables [7]. An implementation of FCHC on the CAM-8 was carried out in 1995 by Alder, Boghosian, Flekkoy, Margolus, and Rothman [22].

functional form of the equilibrium occupancy probability [59]. The drawback of the BGK approximation is that it violates detailed balance, but it has computational advantages over modeling lattice gases at the microscopic scale because of a significant viscosity reduction. Subsequently, a lattice Boltzmann BGK model for compressible fluid dynamics was proposed by Alexander, H. Chen, S. Chen, and Doolen [60] and another lattice Boltzmann BGK model for thermohydrodynamics was proposed by Alexander, Chen, and Sterling [61].

The lattice Boltzmann equation in the BGK approximation has been a useful contribution of the lattice gas community to high-performance computational physics [62].[3] The lattice Boltzmann equation (implemented within one hundred lines of code in a parallel language such as FORTRAN 90) allows one to efficiently model fluids with near second-order convergence using an explicit time-step scheme. Martinez, Matthaeus, S. Chen, and Montgomery compared the lattice Boltzmann BGK method to the well known spectral method and found comparable numerical efficiency in both methods [63]. The lattice Boltzmann method was extended to the simulation of multiphase and multispecies applications by Shan [64, 65, 66, 67], Grunau [68], and Yeomans *et al.* [69, 70, 71]. Because of the practicality of the lattice Boltzmann method, we have explored ways to restore detailed balance, in particular by using an unconditionally stable collision process that uses unitary matrices to produce the outgoing configuration of occupancy probabilities.

Other areas of lattice gas research include: thermohydrodynamics [38, 28, 27, 61, 63], immiscible fluids [9, 37, 72, 73], reaction-diffusion systems [74, 75, 76], magnetohydrodynamics [77, 78, 79, 80], flow through porous media [81, 36], and renormalized kinetic theory [82, 83, 84, 85, 86, 87, 88]. Numerical measurements taken from classical lattice gas simulations are generally in excellent agreement with mean-field theory predictions and, in the rare instance when this is not the case, with more exact field theoretic calculations [82, 85, 88]. Lattice gases simulate physical systems while keeping multiparticle correlations. The phenomenon of long-time tails in the velocity autocorrelation function [89, 90, 91] has recently been observed in lattice gases by KirkPatrick [82] and Brito [83, 85].

A good review of the lattice gas subject, with particular emphasis on interfaces, phase transitions, and multiphase flow, has recently been presented by Rothman and Zaleski [13]. Additionally, a comprehensive bibliography of the subject has been compiled by Doolean [92].

1.4 Lattice-Gas Applications to Multiphase Fluid Dynamics

Microscopic lattice gas models of multiphase fluids were introduced by Chen *et al.* [34] and by Appert and Zaleski [10, 11, 12], and Yepez [14, 15, 16]. It is known that interparticle potentials can be modeled by including a single anisotropic nonlocal interaction in the lattice gas dynamics for discrete momentum exchange between particles. The simplest model of this kind is the Kadanoff-Swift-Ising model [93]. A nonlocal interaction of the type was used in a lattice gas scheme by Appert and Zaleski [10] in 1990 to cause an attractive force between particles giving rise to an athermal liquid-gas phase transition.[4]

To simulate the correct macroscopic dynamics, the interaction range for the momentum exchange must be much smaller than any scale related to the interface region that exists between the two phases in order for the multiphase lattice gas to be operative. For example, the interaction range must be much smaller than the radius of curvature of a drop or bubble and much smaller than the wavelength of a capillary wave or gravity wave travelling along the interface.

In the bulk region, the lattice-gas collision operator for the nonlocal interactions vanishes, and only the local collisions determine the hydrodynamic behavior. Furthermore, the rheology of multiphase dynamics is driven by low Reynolds number flows. The rheology of droplets (for example

[3] The first lattice Boltzmann simulations for three dimensional flows with high Reynolds numbers (about 50,000) were presented in June 1993 at the International Conference on Pattern Formation and Lattice-Gas Automata sponsored by the Fields Institute, Waterloo, Canada.

[4] A *nonthermal* lattice-gas is one with intensive quantities for the pressure and density, but no intensive quantity related to temperature. This is because, a nonthermal lattice-gas is one where all particles move at a single speed and a particle's mass and momentum are uniquely defined, but its energy is not.

diffusive growth, coalescence, or droplet breakup by high shear flows) is a complicated hydrodynamic process yet well approximated as a nonturbulent one. Complex fluid behavior of this sort is characterized by a well-defined local equilibrium that exists throughout the entire fluid volume. The nonlinear behaviors driven by convection or by surface energetics occurs while the multiphase fluid is in local equilibrium everywhere (particularly in the bulk regions) and slowly approaches a global thermodynamic equilibrium. The local equilibrium of the fluid is characterized by a nearly isotropic occupancy of local momentum states. At zeroth order, the fluid is locally at rest with the probability of occupancy being uniformly distributed in momentum space. The nonequilibrium fluid is characterized by a small first-order correction away from the local equilibrium. Momentum slowly diffuses through the fluid system (quantified by the transport coefficient for viscosity) in a random walk fashion.

Classical lattice gases use only a single bit to represent the occupancy of a particle in a local state whereas in molecular dynamics codes a few hundred bits are used (six floating-point numbers for position and momentum). To do physical modeling at the microscopic and mesoscopic scales, molecular dynamics is the appropriate modeling tool. However, at large hydrodynamic scales, a classical lattice gas is the modeling tool of choice. Predicting the hydrodynamics behaviors of microemulsions (three species fluid of water, oil, and a surfactant with dipolar molecules) have demonstrated that lattice gases are more efficient that molecular dynamics. No competing high level scheme is known for microemulsions. The microemulsion lattice gases have been studied by Boghosian, Coveney, and Emerton [24]. They have mapped out the transition between phases as a function of surfactant concentration and domain growth laws, which have been found to be in good agreement with experiment [25]. Lattice Boltzmann simulations of microemulsions has been done by Yeomans *et al.* [94].

1.5 Limitations and Drawbacks of Classical Lattice Gases

Far away from equilibrium where local equilibrium conditions on the particle configurations are violated, classical lattice gases behave in unphysical ways. These behaviors are not signs of instabilities, but indicate that far away from equilibrium artifacts caused by the discreteness of the microscopic dynamics can arise at the macroscopic scale.

The classical lattice gas is like its classical molecular dynamics counterpart. The available number of particles, per computer simulation, is still far too few (on the order of billions) compared with the vast numbers of particles in any natural situation (on the order of Avagadro's number) it is trying to represent. Classical lattice gases fail to adequately capture turbulence within large-scale hydrodynamics motions because of limitations of available memory resources in classical computers. Orszag and Yakhot have consequently argued that classical lattice gases are not as efficient as the competing high level CFD methods which make more efficient use of available memory [95].

As well as limited in spatial and temporal resolution, classical lattice gases possess noisy fluctuations [33]. These fluctuations are a mechanism whereby the lattice gas explores different metastable states [13]. They have the negative aspect of effectively reducing the classical simulation's macroscopic scale. If the system is ergotic[5], we have one of two choices to remove the noise in any measurement. We can either increase the spatial size of the lattice to allow for more spatial and temporal coarse-grain averaging or increase the number of sample runs with different initial conditions. The latter is a means of ensemble averaging. In either case, significant computational resources must be expended to remove noisy fluctuations instead of expending these resources on increasing the resolution of the simulation.

Some possibilities have been explored to try to avoid the noisy fluctuations in classical lattice gas simulations. As mentioned above, in lattice Boltzmann simulations, noisy fluctuations in the system

[5] A lattice gas is said to be *ergotic* if numerical results obtained by course-grain averaging over a single large microscopic realization are identical to the numerical results obtained by ensemble averaging over many microscopic realizations.

have smaller sizes than in a system governed by microscopic lattice-gas rules. Yet the lattice Boltzmann method suffers from numerical instabilities typically encountered in finite-difference methods. The reason for this comes about by the method's lack of detailed balance, or even its lack of the weaker condition of semi-detailed balance, in its BGK collision operator.[6] Since it is essentially a first-order finite-difference method [63], the explicit lattice Boltzmann BGK method is not more efficient than state-of-the-art implicit and second-order convergent computational fluid dynamics methods, for example methodes employing either multiscaling or curvilinear adaptive meshing.

1.6 The Navier-Stokes Equation

The long wavelength hydrodynamic behavior of a many-body system of particles can be modeled at the macroscopic scale by an effective field theory, a set of coupled partial differential equations. The smooth fields of mass density, ρ, and flow velocity, $\vec{v}$, obey a mass continuity equation and a viscous Navier-Stokes fluid equation of motion. There is also a parabolic heat equation for the energy density, yet for simplicity, I will not consider the heat equation here, and instead I shall consider an athermal fluid.

Because the mass increase within a region $\mathcal{R}$ is entirely accounted for by the flux of particles into $\mathcal{R}$ through its boundary $\partial\mathcal{R}$, the ρ and $\vec{v}$ fields obey the continuity equation

$$\partial_t \rho + \partial_i(\rho v_i) = 0. \tag{1.1}$$

This is the first equation of motion. Here, the shorthand notation for partial derivatives is used: $\partial_t \equiv \partial/\partial_t$ and $\partial_i \equiv \partial/\partial x_i$. The field equation embodying Newton's second law, for a region $\mathcal{R}$ expressing the change in the momentum density in terms of the stress applied at the boundary $\partial\mathcal{R}$, is Euler's equation

$$\partial_t(\rho v_i) + \partial_j \Pi_{ij} = 0. \tag{1.2}$$

Now following Landau and Lifshitz [96], the momentum flux density tensor is written as[7]

$$\Pi_{ij} = P\delta_{ij} + \rho v_i v_j - \eta(\partial_i v_j + \partial_j v_i - \frac{2}{D}\partial_k v_k \delta_{ij}) - \zeta \delta_{ij}\partial_k v_k. \tag{1.3}$$

The viscous stress tensor is $\sigma'_{ij} = \eta(\partial_i v_j + \partial_j v_i - \frac{2}{D}\partial_k v_k \delta_{ij}) + \zeta\delta_{ij}\partial_k v_k$, where η and ζ are the transport coefficients for the shear viscosity and bulk viscosity, respectively, and D is the number of spatial dimensions of the system. The first two terms in Equation (1.3) represent the *ideal part* of the momentum flux density tensor, which is sum of the pressure term, P, plus the convective term, $\rho\vec{v}\vec{v}$, which is nonlinear in the velocity.

In general the pressure, P, is a function of the mass density field, $\rho = \rho(\vec{x}, t)$, and for a thermal fluid it also is a function of the temperature field, $T = T(\vec{x}, t)$. The pressure tensor is diagonal because the fluid is *isotropic*. $P = P(\rho, T)$ is termed the *equation of state*. For a *neutral fluid* comprised of independently moving particles, the pressure depends linearly on the mass density, $P = c_s^2\rho$, where c_s is the *speed of sound* in the fluid. In a thermohydrodynamic system, the sound speed is temperature dependent, $c_s = \sqrt{\frac{k_{\rm B}T}{m}}$ (where $k_{\rm B}$ is the Boltzmann constant and m is the mass of a single particle). In this case the pressure obeys the well known *ideal gas law*, $P = nk_{\rm B}T$, where $n = \frac{\rho}{m}$ is the particle number density. For an athermal hydrodynamic system (one where

[6] Mass and momentum are only conserved to within the precision of the floating-point representation. If the value of the single-particle distribution function at some site is close to either zero or one, it is possible that the occupancy probabilities there will become either negative or greater than one because of numerical round-off errors . When either of these situations arise, the lattice Boltzmann simulation will eventually become unstable everywhere and the values of the distribution function will diverge until a numerical underflow or overflow event occurs. Usually the BGK collision operator becomes unstable in a region with a high density gradient, for example at an interfacial boundary, or in a region a with a high velocity shear.

[7] For non-divergent flow ($\partial_j v_j = 0$) in the incompressible fluid limit, Equation (1.3) is $\Pi_{ij} = P\delta_{ij} + \rho v_i v_j + \eta(\partial_i v_j + \partial_j v_i)$. Furthermore, the term $\eta\partial_i v_j$ vanishes in the Euler equation in this limit.

the system is at uniform homogeneous temperture, and where heat transport is neglected), c_s is a constant.

Substituting Equation (1.3) into Euler's equation Equation (1.2), gives us the second equation of motion for a viscous isotropic fluid

$$\rho\left(\partial_t v_i + v_j \partial_j v_i\right) = -\partial_i P + \rho\nu\partial^2 v_i + \left(\zeta + \frac{\eta}{D}\right)\partial_i\partial_j v_j. \tag{1.4}$$

This is the called the *Navier-Stokes* equation. In Equation (1.4), η is the *shear viscosity* and ζ is the *bulk viscosity*. The transport coefficient for momentum diffusion, $\nu \equiv \frac{\eta}{\rho}$, is the *kinematic viscosity*. It gives a measure for the rate of decay of local shears in the fluid and determines how fast a perturbed fluid will relax from an anisotropic flow profile at the macroscopic scale to an isotropic steady state profile. Both the shear viscosity and the bulk viscosity cause damping of compressional waves in the mass density field. The shear viscosity alone causes damping of shear waves in the momentum density field. In general, for a nonisotropic fluid, there may also exist a *cubic viscosity*. However, in our case we shall deal with isotropic fluids where the shear and cubic viscosities coincide.

1.7 Dimensionless Numbers

Let L and T denote the characteristic length and time scales, respectively, of a hydrodynamic scale fluctuation. That is, L and T are quantities characterizing the fluid's configuration at the macroscopic scale. Examples of the characteristic length scale for hydrodynamic flow are the wavelength of a compressional wave in the mass density field, the wavelength of a shear wave in the momentum density field, or the diameter of a fluid vortex. The mean free path is the average distance a particle travels between collisions. Let λ and τ denote the mean-free length and time, respectively, characterizing the microscopic particle collisions. Relevant hydrodynamic quantities are the

- *characteristic flow speed*, $u \sim \frac{L}{T}$;
- *sound speed*, $c_s \sim \frac{\lambda}{\tau}$;
- *shear viscosity*, η (and the *kinematic viscosity*, $\nu \equiv \frac{\eta}{\rho} \sim \frac{\lambda^2}{\tau}$); and,
- *bulk viscosity*, ζ.

The relevant dimensionless quantities are the

- *Knudsen number*, Kn, defined as the ratio of the mean-free path to the characteristic length scale ($\mathrm{Kn} \equiv \frac{\lambda}{L}$);
- *Strouhal number*, Sh, defined as the ratio of the mean-free time to the characteristic time scale ($\mathrm{Sh} \equiv \frac{\tau}{T}$);
- *Mach number*, M, defined as the ratio of the characteristic velocity to the sound speed ($\mathrm{M} \equiv \frac{u}{c_s}$);
- *Reynolds number*, Re, defined as the ratio of the product of the characteristic velocity times characteristic length to the kinematic viscosity ($\mathrm{Re} \equiv \frac{uL}{\nu} \sim \frac{\mathrm{M}}{\mathrm{Kn}}$); and,
- *fractional mass density variation*, $\frac{\delta\rho}{\rho}$.

Chapter 2

An Analytical Method for Predicting Macroscopic Behavior

Table 2.1: Lattice-Gas Model Symbols

Symbols	**Names**
ℓ	microscopic cell size
ℓ_s	mesoscopic cell size
τ	time unit
m	single particle mass
c	velocity unit ($\frac{\ell}{\tau}$)
D	spatial dimension
B	lattice coordination number
a	directional index (1,2,..., B)
i, j, k, l	spatial indices
e_{ai}	displacement vectors

2.1 Mesoscopic Scale

2.1.1 Derivation of the Linearized Kinetic Equation

Define the *occupancy probability* of a local state, $f_a \equiv \langle n_a \rangle$, as an ensemble average over independent microscopic realizations of the lattice-gas system. In the *mean-field limit* approximate, the particle occupancies f_a's are considered uncorrelated at all times. Neglecting the particle-particle correlations is known as the *Boltzmann molecular chaos* assumption (or the *Stosszahlansatz*). This approximation allows us to estimate the macroscopic quantities, such as the damping constants, and the shear and bulk viscosities (and the equation of state in multiphase lattice gases). We describe the mesoscopic dynamics of a lattice-gas system at the mesoscopic scale by the lattice Boltzmann equation

$$f_a(\vec{r} + \ell \hat{e}_a, t + \tau) = f_a(\vec{r}, t) + \Omega_a^{\text{meso}}(f_*), \tag{2.1}$$

where the momentum index a ranges from 0 to $B - 1$ specifying the *local states* at each site of the lattice. The superscript on the collision term, Ω_a^{meso}, indicates that its functional form is to be expressed at the *mesoscopic scale*. The asterisk on occupation probability, f_*, in the collision term

htbp

Table 2.2: Glossary of Single-Speed Lattice Gas Variables (L=1)

Variables	**Names**
n_a	microscopic number occupation variable for a local state
$\vec{p}$	microscopic momentum
Ω_a	microscopic collision operator
s	microscopic configuration of particles at a site
$T_{ss'}$	transition matrix
f_a	mesoscopic probability of occupation of a local state, $\langle n_a \rangle$
Ω_a^{meso}	mesoscopic collision operator
J_{ab}	Jacobian matrix, $\frac{\partial \Omega_a}{\partial f_b}$
$\lvert\alpha\rangle$	eigenkets of J
κ_α	eigenvalues of J
c_s	macroscopic sound speed
P	macroscopic pressure
ρ	macroscopic density
$\vec{v}$	macroscopic velocity
Π_{ij}	macroscopic momentum flux density tensor
η	shear viscosity
ν	kinematic viscosity, $\frac{\eta}{\rho}$

indicates that Ω_a^{meso} depends on all the local states in the system and not just f_a. In the *mean-field limit*, $\Omega_a^{\text{meso}}(f_*) = \Omega_a^{\text{mf}}(f_0, f_1, \ldots, f_{B-1})$ depends only on the local states at the lattice site $\vec{r}$.

The parameters ℓ and τ are the cell size and the update time, respectively, of the spacetime lattice at the mesoscopic scale. The parameter B equals the number of local states at a site in a Bravais lattice. The vectors $\vec{e}_a$ are displacement vectors whose length corresponds to the speed of the particles, since each local state may be occupied by a particle with momentum $\vec{p} \equiv mc\vec{e}_a$.

2.1.2 The Approach to Steady-State Equilibrium

The system is said to be in *steady-state equilibrium* (which may also be called *thermodynamic equilibrium*) when the collision term in the lattice Boltzmann equation vanishes

$$\Omega_a^{\text{meso}}(f_*^{\text{eq}}) = 0, \tag{2.2}$$

where f_a^{eq} is equilibrium occupation probabilities. Therefore, at steady-state equilibrium, the occupancy probabilities are unchanging over time. The distribution along the momentum directions of the particle occupancies are uniform, so the local configurations are perfectly symmetric, and Ω_a^{meso} cannot cause any further changes.

Let us predict the non-equilibrium behavior of the lattice-gas system when it is nearby and approaching steady-state equilibrium. Since continuous macroscopic fields for the mass and momentum densites are defined for the lattice-gas system in the continuum limit, by Equations (2.34) and (2.35), we can characterize the system using the dimensionless quantities traditionally used to characterize fluid systems. Given the *law of similarity*[1], if the macroscopic scale behavior of the lattice gas is fluid-like, then it may be compared to a natural fluid characterized by the same dimensionless quantities.

Several dimensionless quantities (the Knudsen, Strouhal, Mach, and Reynolds numbers, and fractional mass density variation) allow us to quantify how close the system is to steady-state equilibrium. At steady-state equilibrium all the dimensionless numbers vanish (only the Mach number

[1] See page 56 of Fluid Mechanics by Laudau and Lifshitz [96].

may be nonzero at equilibrium if there is a global uniform background flow, however this can be avoided by an appropriate choice of the Galilean frame-of-reference). In nonequilibrium situations far from steady-state, Kn, Sh, M, and $\frac{\delta\rho}{\rho}$ are order unity.

Hydrodynamic behavior is attained in the long wavelength limit where Kn and Sh are close to zero. *Viscous* hydrodynamic behavior is attained in the long wavelength limit when Sh $\sim$ Kn^2 and $\frac{\delta\rho}{\rho} \sim$ Kn. This is called *diffusive ordering* which is characteristic of random walk processes.[2]. *Incompressible* viscous hydrodynamics occurs when we also have M $\sim$ Kn so that Re $\sim \mathcal{O}(1)$ and $\frac{\delta\rho}{\rho} \sim$ Kn^2. A procedure for linearizing the mesoscopic Boltzmann equation, and comparing the resulting dispersion relations to the solution of the effective field theory equations of motions, is given below in Section 2.1.3. The procedure involves a series expansions in $\frac{\delta\rho}{\rho}$. The standard Mach number expansion of the probability of occupancy is used [3]. Then, a Chapman-Enskog procedure, given in Section 2.2.2, which is necessary for the derivation of the macroscopic equations of motion involves perturbative expansions in Kn and Sh, given in Section 2.2.3.

At $t = \infty$, an infinite lattice-gas system completely relaxes to steady-state equilibrium, where the mass density field is uniformly constant. The steady-state equilibrium occupation probability, denoted by d, of every local state are all the same $f_a(\vec{x}, \infty) = d$, for all a and all $\vec{x}$. For a lattice of finite size, the number of phasespace points is also finite, although extremely large. The number of phasespace points equals 2^{BV}, where B is the number of local states per site and V is the total number of sites. Hence the Poincaré recurrence time, which is the number of phasespace points of a closed loop trajectory, is also finite and the state of the finite-lattice gas system is not defined at $t = \infty$. Hence, we may instead say that the lattice-system has completely relaxed to a steady state on a time scale much much larger than the characteristic time $(\frac{\tau}{\mathrm{Sh}})$ for the largest hydrodynamic scale fluctuation.

2.1.3 Linearized Lattice Boltzmann Equation

Our first step towards analyzing the nonsteady-state behavior of the system will be to expand f_a^{noneq} about d. We write the occupancy probability as a constant part ($d \equiv \frac{\rho}{mB}$) and a fluctuating part $\delta f_a(\vec{x}, t) \ll d$

$$f_a(\vec{x}, t) = d + \delta f_a(\vec{x}, t). \tag{2.3}$$

We can also expand the collision term about steady-state equilibrium

$$\Omega_a^{\mathrm{meso}}(f_*) = \Omega_a^{\mathrm{meso}}(f_*^{\mathrm{eq}}) + \delta\Omega_a^{\mathrm{meso}}. \tag{2.4}$$

Now the first term on the R.H.S. vanishes according to Equation (2.2) and the second term on the R.H.S. arises because of fluctuations in the probability of occupancies of all the local states in the entire system.

At the mesoscopic scale, we regard each of the occupancy probabilities, f_a, as a continuous variable. The basic approach is that Ω_a is a continuous and differentiable function of the occupation variables. With this understanding, using the chain rule, we can write the collision term Equation (2.4) as follows

$$\Omega_a^{\mathrm{meso}}(f_*^{\mathrm{eq}}) = \delta\Omega_a^{\mathrm{meso}} = \sum_{b=1}^{B} \frac{\partial\Omega_a^{\mathrm{meso}}}{\partial f_b}\bigg|_{f_*=d} \delta f_b + \mathcal{O}(\delta f^2). \tag{2.5}$$

Using Equations (2.3) and (2.5), we can write the lattice Boltzmann equation Equation (2.1) in linearized form

$$\delta f_a(\vec{x} + \ell_s \hat{e}_a, t + \tau) = \delta f_a(\vec{x}, t) + J_{ab}\delta f_b(\vec{r}, t), \tag{2.6}$$

[2] See Figure 3.9 using the classical 1D3Px model to illustrate diffusive ordering that is characteristic of lattice-gas fluids. Furthermore, a tagged particle in a lattice gas undergoes a random walk, and the observed diffusive behavior of tagged-particles in lattice-gas simulations agrees well with analytical results [97, 29]

where the *Jacobian of the collision term* is defined as

$$J_{ab} \equiv \left.\frac{\partial \Omega_a^{\text{meso}}}{\partial f_b}\right|_{f_*=d}. \tag{2.7}$$

Let $\tilde{f}_a(\vec{k},\omega)$ denote the discrete Fourier transform of the occupation probability $f_a(\vec{x},t)$. Then taking the discrete Fourier transform of the linearized Boltzmann equation Equation (2.6) we obtain the following characteristic equation

$$e^{i(\ell_s \hat{e}_a \cdot \vec{k} + \omega\tau)} \delta \tilde{f}_a(\vec{k},\omega) = \delta \tilde{f}_a(\vec{k},\omega) + J_{ab} \delta \tilde{f}_b(\vec{k},\omega), \tag{2.8}$$

which we rewrite as

$$\left[\left(e^{i(\ell_s \hat{e}_a \cdot \vec{k} + \omega\tau)} - 1\right)\delta_{ab} - J_{ab}\right] \delta \tilde{f}_b(\vec{k},\omega) = 0. \tag{2.9}$$

Therefore, we have the following matrix equation

$$\mathbf{M}\ \delta\tilde{\mathbf{f}} = 0, \tag{2.10}$$

where $\tilde{\delta}\mathbf{f} = (\tilde{\delta} f_0, \tilde{\delta} f_1, \ldots, \tilde{\delta} f_{B-1})$ and the components of the square matrix $\mathbf{M}$ are

$$M_{ab} \equiv \left(e^{i(\ell_s \hat{e}_a \cdot \vec{k} + \omega\tau)} - 1\right)\delta_{ab} - J_{ab}. \tag{2.11}$$

Solving Equation (2.10) gives us the dispersion relations for the system obeying what is called *generalized hydrodynamics*. The generalized hydrodynamics for classical lattice-gas systems have been previously worked out [30, 98]. The development given here for the lattice-gas system follows Das and Ernst's treatment of a classical lattice-gas system [30]. However, in the present treatment, I do not use differential point form notation for mesoscopic fields (since technically this is unwarranted and allowed only in the continuum limit). Instead, to be absolutely rigorous, I have applied the discrete Fourier transform to the mesoscopic field to obtain Equations (2.10) and (2.11). So up to this point in the analytical treatment, I have not invoked the continuum limit.

2.1.4 Dispersion Relations

To solve Equation (2.10) for the dispersion relation $\omega = \omega(\vec{k})$, we must find the B roots of the secular determinant of the matrix $\mathbf{M}$ [30, 98]. The solution can be found analytically for the 1D3Px lattice gas and numerically for more complicated lattice gases. In general, there are two types of long wavelength excitations ($\vec{k} \to 0$), and they are called *hard kinetic modes* and *soft hydrodynamic modes*.

In the long-wavelength limit, the kinetic modes are nonvanishing at first order. The kinetic modes decay rapidly in the lattice-gas system because of a positive imaginary part in the eigenvalue spectrum of ω, ($\text{Im}(\omega) > 0$), at $k = 0$. In contrast, the soft hydrodynamic modes decay over a long-time scale. They are associated with eigenvalues that vanish in the long-wavelength limit, ($\text{Im}(\omega) = 0$), at $k = 0$. These vanishing eigenvalues in turn are associated with the conserved quantities in the lattice-gas system.

In the long-wavelength limit, $k \sim 0$, the dispersion relation for the 1D3Px lattice-gas corresponds to a damped sound mode

$$\omega(\vec{k}) = \pm c_s k + i\Gamma(\rho)k^2. \tag{2.12}$$

The real part of ω is linear in the wave number. Since $\text{Re}(\omega)$ is linear in the wave number, the sound mode excitation propagates at the sound velocity corresponding to the slope, which is denoted here by c_s. Furthermore, the sound mode is damped in the *viscous hydrodynamic regime* characterized by diffusive ordering where the dispersion relation is parabolic in wavenumber, $\text{Im}(\omega) \sim \mathcal{O}(k^2)$. In general, in a single-speed lattice gas, the decay of the hydrodynamic modes depends on shear viscosity and sound damping (there is no mode related to bulk viscosity).

2.1.5 Criterion for Deviations from Local Equilibria

At local equilibrium, we assume that the occupancies of the local states at each site in the system are isotropic. This is called the *subsonic limit*. A stronger definition of the subsonic limit is when the fractional variation of the occupancy probabilities, $|\delta f_a|/f_a^{\rm eq}$, at all lattice sites, are assumed to be uniformly distributed along all the momentum directions, $1 \leq a \leq B$. Hence, the criterion for a fractional mass density variation on the order of the Knudsen number, can be expressed as[3]

$$\frac{|\delta f_a|}{f_a^{\rm eq}} \sim \frac{\lambda}{BL}. \tag{2.13}$$

The maximum size of the simulation volume is limited by the amount of physical computational resources available. In a microscopic lattice-gas simulation, the occupation probabilities, f_a, must be determined by either partitioning the maximum size simulation into ensemble realizations or coarse-grain blocks. Let us, for the moment, revisit the subject of averaging over the microscopic quantities to obtain the mesoscopic values. There are more details to discuss.

In ensemble averaging, many realizations of the lattice-gas system, which are identical at the macroscopic scale, are computed independently. Measurements are separately made from each realization, and all the resulting measurements are then averaged. For example, the state of the $\alpha^{\rm th}$ qubit is measured for each copy of the system, which results in a series of 1's and 0's, and the average value is an estimate of f_α. In coarse-grain averaging, one measures the occupancy of all the local states, occupied by a particle with momentum $mc\hat{e}_a$, at all the sites within a spacetime block of a large microscopic system. Again, this results in a series of 1's and 0's, which are then averaged to estimate $f_a(\vec{X}, T)$, where say $\vec{X}$ and T denote the coordinates of the centroid of a spacetime block within the superlattice.

In either case, whether ensemble or coarse-grain averaging is employed, all the available computational resources are expended. However, the numerical results can be quite different, for two reasons: because lattice-gas systems obey diffusive ordering and because of renormalization effects arising from particle-particle correlations.

Let us first consider the consequences of diffusive ordering. If one doubles the system size, $L \to 2L$, one must quadruple the simulation time, $T \to 4T$, to evolve to a macroscopic state similar to the one obtained by running a simulation of size L for time T. Consequently, if the fixed amount of computational resource is partitioned to do ensemble averaging, then many "small" systems are simulated which "rapidly" relax towards steady-state equilibrium. If the fixed amount of computation resource is partitioned to do coarse-grain averaging, then one "large" system is simulated which "slowly" relaxes towards steady state. Therefore, estimates can be made more quickly using ensemble averaging, but only in those situations were particle-particle correlations can be neglected.

This brings us to the next issue of renormalization. In a large system simulation, there is sufficient time for many particle collision events to occur allowing the particle occupancies to become correlated. These particle-particle correlations, in certain situations, may have an appreciable effect on the value of the transport coefficients [88]. One enumerates all *connected diagrams* corresponding to the pathways by which outgoing particles, initially correlated by a collision, move through the system, interact with other particles, and eventually return as incoming particles to a final collision event. Each connected diagram corresponds to a term in an asymptotic series expansion of the collision operator, which is summed to give a *renormalized* collision operator. If the ultimate aim of is to estimate a transport coefficient, which strongly depends on particle-particle correlations, then coarse-graining averaging must be used [99, 88].

[3] Suppose, as a concrete example, that an initial nonequilibrium state of the system is chosen with a characteristic feature size on the order of say one hundred lattice grid units, $L \sim 100\ell$. Next, suppose the mean-free path length is on the order of the size of a single primitive lattice cell, $\lambda \sim \ell$. If the fractional mass density variation, which must be on the order of the Knudsen number is $\frac{\delta\rho}{\rho} \sim \frac{\lambda}{L} \sim 0.01$, then the lattice gas would accurately model the dynamical fluid behavior in the regime of incompressible viscous hydrodynamics. Continuing the example, if $B = 6$ then $|\delta f_a|/f_a^{\rm eq} \sim 0.002$.

In either case, it is necessary to satisfy the criterion that $(\delta f_a/f_a^{\rm eq}) \sim \mathcal{O}(\mathrm{Kn})$ or smaller for all a. If this criterion is satisfied, the linearized lattice Boltzmann equation Equation (2.6) can accurately describe Navier-Stokes hydrodynamics. And this is a stronger requirement then $\frac{\delta\rho}{\rho} \sim \mathcal{O}(\mathrm{Kn})$. The requirement that $(\delta f_a/f_a^{\rm eq}) \sim \mathcal{O}(\mathrm{Kn})$ for viscous hydrodynamics (or the more stringent requirement that $(\delta f_a/f_a^{\rm eq}) \sim \mathcal{O}(\mathrm{Kn}^2)$ for incompressible viscous hydrodynamics) implies a lower bound for the number of states used in an ensemble average or for the minimum size of the spacetime block used in a coarse-grain average. All these considerations, usually applied to the classical lattice-gas method, are also relevant to quantum lattice-gas simulations [100, 101], which are not reviewed here.

2.2 Macroscopic Scale

2.2.1 Eigensystem of the Linearized Collision Operator

In the long wavelength ($\vec{k} \to 0$) limit, the characteristic equation Equation (2.9) reduces to the simple form

$$[(e^{\omega\tau} - 1)\mathbf{1} - \mathbf{J}]\ \delta\tilde{\mathbf{f}} = 0. \tag{2.14}$$

Expanding to first order in Sh (second order in ε) this become the eigenvalue equation

$$\mathbf{J}\ \delta\tilde{\mathbf{f}} = \omega\tau\delta\tilde{\mathbf{f}} + \mathcal{O}(\varepsilon^3). \tag{2.15}$$

Therefore, in the long-wavelength and low-frequency limits, the eigenvalues of J determine possible values for ω and in turn the hydrodynamic and kinetic behavior of the lattice-gas system. This eigenvalue problem is analytically solvable, without the need for any numerical treatment as is needed for finding the $\vec{k}$-dependent roots of the secular determinant of the matrix M in Equation (2.11).

Consider the following eigenvalue equation

$$J_{ab}\xi_b^\alpha = \kappa_\alpha \xi_a^\alpha, \tag{2.16}$$

with eigenvectors ξ^α and eigenvalues κ_α, where $\alpha = 1, \ldots, B$.[4] Let us see why there will be as many zero eigenvalues as there are conserved quantities in the lattice gas dynamics. For convenience, we will use ket notation where $|\alpha\rangle \equiv (\xi_1^\alpha, \xi_2^\alpha, \ldots, \xi_B^\alpha)$ and $|\delta\tilde{f}\rangle \equiv (\delta\tilde{f}_1, \delta\tilde{f}_2, \ldots, \delta\tilde{f}_B)$. We can write J as follows

$$J = \sum_{\alpha=1}^{B} \kappa_\alpha |\alpha\rangle\langle\alpha|, \tag{2.19}$$

so Equation (2.15) becomes

$$\sum_{\alpha=1}^{B} \kappa_\alpha |\alpha\rangle\langle\alpha|\delta\tilde{f}\rangle = \omega\tau|\delta\tilde{f}\rangle. \tag{2.20}$$

All the scalars $\langle\alpha|\delta\tilde{f}^{(1)}\rangle$ for which $\kappa_\alpha = 0$ have no effect on the dynamics since $J|\delta\tilde{f}\rangle = 0$ and so correspond to the conserved quantities of the system. The set of eigenvectors with degenerate eigenvalue of zero span what is called the *hydrodynamic space*, which I denote by $\mathcal{H}$. The remaining set of eigenvectors (with nonzero eigenvalues) span what is called the *kinetic space*, which I denote

[4] The problem is simplified if J is circulant [1]. The components of J can be specified by the difference of the indices, $J_{ab} = J_{a-b}$. Hence, we make the ansatz that the eigenvectors ξ^α have the following form

$$\xi_a^\alpha = e^{2\pi i a\alpha/B}. \tag{2.17}$$

Then inserting Equation (2.17) into Equation (2.16) and taking $m = a - b$, gives a solution for the eigenvalues

$$\kappa_\alpha = \sum_{m=1}^{B} J_m e^{2\pi i m\alpha/B}. \tag{2.18}$$

as $\mathcal{K}$. Therefore J can be explicitly written as a linear combination over eigenvectors in the kinetic space

$$J = \sum_{\alpha \in \mathcal{K}} \kappa_\alpha |\alpha\rangle\langle\alpha|. \tag{2.21}$$

In an athermal system, there are $1 + D$ conserved quantities, the mass plus the momentum for each dimension of the space. So $\mathcal{H}$ is a $D+1$ dimensional space and $\mathcal{K}$ is a $B - D - 1$ dimensional space. Let us denote the kinetic eigenkets as follows, $|D+2\rangle, |D+3\rangle, \ldots, |B\rangle$, which span the kinetic subspace $\mathcal{K}$. Then, the generalized inverse of J is defined over $\mathcal{K}$ as follows

$$J^{-1} = \underbrace{(|D+2\rangle\ |D+3\rangle \cdots |B\rangle)}_{B\times K \text{ matrix}} \underbrace{\begin{pmatrix} \frac{1}{\kappa_{D+2}} & 0 & \cdots & 0 \\ 0 & \frac{1}{\kappa_{D+3}} & \cdots & 0 \\ \vdots & & \ddots & \\ 0 & \cdots & & \frac{1}{\kappa_B} \end{pmatrix}}_{K\times K \text{ matrix}} \underbrace{\begin{pmatrix} \langle D+2| \\ \langle D+3| \\ \vdots \\ \langle B| \end{pmatrix}}_{K\times B \text{ matrix}}. \tag{2.22}$$

From Equation (2.22), it follows by construction that

$$J^{-1}|\alpha\rangle = \frac{1}{\kappa_\alpha}|\alpha\rangle, \tag{2.23}$$

for $|\alpha\rangle \in \mathcal{K}$.

Within $\mathcal{K}$ there exists the *viscous subspace*, $\mathcal{V} \subset \mathcal{K}$ characterized by the degenerate eigenvalue κ_η. Because the collisional process is invariant under the finite point-group symmetries of the Bravais lattice, consequently there is a lack of preference in direction for momentum diffusion in the system. Hence, there is a subspace of $\mathcal{K}$ characterized a degenerate eigenvalue which contributes positively to the shear and bulk viscosities.

A ket $|e_i e_j\rangle$ may be formed from the dyadic product $e_{ai}e_{aj}$. The ket $|\ e_i e_j\rangle$ resides in $\mathcal{V}$. It is an eigenket of the generalized inverse of the Jacobian of the collision operator, J^{-1}, and has eigenvalue $\frac{1}{\kappa_\eta}$. That is, for a hydrodynamic lattice-gas fluid

$$J^{-1}|e_i e_j\rangle = \frac{1}{\kappa_\eta}|e_i e_j\rangle. \tag{2.24}$$

The identity Equation (2.24) will be needed in the following section.

2.2.2 Chapman-Enskog Expansion

The characteristic equation Equation (2.9) of the linearized lattice Boltzmann equation

$$\left[\left(e^{\ell_s \hat{e}_a \cdot \vec{k} + \omega\tau} - 1\right)\delta_{ab} - J_{ab}\right]\delta\tilde{f}_b(\vec{k},\omega) = 0$$

is an approximate description of the mesoscopic particle dynamics since the collision term on the R.H.S. has been expanded to first order about the equilibrium value of the occupation probability. In this approximation, the collision term, J_{ab}, acts as a linear operator on the local configuration $\delta\mathbf{f}$. I would now like to expand the L.H.S. of this characteristic equation. To do so, let us use ε as a small expansion parameter, $\varepsilon \ll 1$. In the viscous hydrodynamic regime, this expansion parameter is the Knudsen number, $\mathrm{Kn} \simeq \hat{e}_a \cdot \vec{k} = \ell_s|k| \sim \varepsilon$. And, because of diffusive ordering, the Strouhal number is $\mathrm{Sh} \simeq \omega\tau \sim \varepsilon^2$. We expect Equation (2.9) is an appropriate description of the mesoscopic dynamics so long as the nonequilibrium occupation probabilities are close enough to their equilibrium values so that the action of the linearized collision term, J_{ab}, is sufficient to cause any such nonequilibrium configuration to relax back to an equilibrium configuration.

Begin by expanding Equation (2.9) to first order in ε

$$(i\ell_s \hat{e}_a \cdot \vec{k}\delta_{ab} - J_{ab})\delta\tilde{f}_b \simeq 0. \tag{2.25}$$

The basic approach is that the deviations, $\delta\tilde{f}_a$, of the occupation probability can be expanded in powers of ε

$$\delta\tilde{f}_a = \delta\tilde{f}_a^{(0)} + \delta\tilde{f}_a^{(1)} + \mathcal{O}(\varepsilon^2), \tag{2.26}$$

where $\delta\tilde{f}_a^{(0)} \sim \varepsilon$ and $\delta\tilde{f}_a^{(1)} \sim \varepsilon^2$. The superscript on $\delta\tilde{f}^{(0)}$ denotes that it is a deviation from the steady-state equilibrium d due to bulk motion of the fluid. The superscript on $\delta\tilde{f}^{(1)}$ denotes that it is a deviation due to spatial gradients in the bulk profile. We require that the largest Mach number at any point in the system must be small, M $\ll 1$, that $\delta\tilde{f}^{(0)} \sim M \sim \varepsilon$. We can insert Equation (2.26) into the first order ε-expansion of the characteristic equation Equation (2.25), $J_{ab}\delta\tilde{f}_b^{(0)} = 0$, and we equate the two $\mathcal{O}(\varepsilon^2)$ terms

$$i\ell_s\hat{e}_a \cdot \vec{k}\delta\tilde{f}_a^{(0)} = J_{ab}\delta\tilde{f}_b^{(1)}. \tag{2.27}$$

Since J has a well-defined generalized inverse, we can invert the Jacobian matrix according to Equation (2.22) to solve for the second order correction to the occupation probability

$$\delta\tilde{f}^{(1)} = i\ell_s J_{ab}^{-1}\hat{e}_b \cdot \vec{k}\delta\tilde{f}_b^{(0)}. \tag{2.28}$$

Therefore, using the basic approach of the Chapman-Enskog expansion Equation (2.26), we have the result that

$$\delta\tilde{f}_a = [\delta_{ab} + i\ell_s J_{ab}^{-1}\hat{e}_b \cdot \vec{k}]\delta\tilde{f}_b^{(0)} + \mathcal{O}(\varepsilon^3). \tag{2.29}$$

In the continuum limit, we are justified in taking the inverse Fourier transform of Equation (2.29), which gives the fluctuating part of the non-equilibrium probability occupancy in differential point form

$$\delta f_a(\vec{x}, t) = [\delta_{ab} + \ell_s J_{ab}^{-1}\hat{e}_b \cdot \nabla]\delta f_b^{(0)}(\vec{x}, t) + \mathcal{O}(\varepsilon^3). \tag{2.30}$$

Then using Equation (2.3), the probability of occupancy in the continuum limit is

$$f_a(\vec{x}, t) = [\delta_{ab} + \ell_s J_{ab}^{-1}\hat{e}_b \cdot \nabla]f_b^{(0)}(\vec{x}, t) + \mathcal{O}(\varepsilon^3). \tag{2.31}$$

We can insert the standard Mach number expansion [3] into Equation (2.31). After some algebraic manipulation, the result is

$$f_a = d[1 + \frac{D}{c}e_{ai}v_i + g\frac{D(D+2)}{2c^2}Q_{aij}v_iv_j + \tau D J_{ab}^{-1}e_{bi}e_{bj}\partial_i v_j] + \mathcal{O}(M^3). \tag{2.32}$$

Using the identity Equation (2.24), that $J_{ab}^{-1}e_{bi}e_{bj} = \frac{1}{\kappa_\eta}e_{ai}e_{aj}$, Equation (2.32) becomes

$$f_a = d[1 + \frac{D}{c}e_{ai}v_i + g\frac{D(D+2)}{2c^2}Q_{aij}v_iv_j - \frac{\tau D}{\kappa_\eta}e_{ai}e_{aj}\partial_i v_j] + \mathcal{O}(M^3). \tag{2.33}$$

The approximation Equation (2.33) is a good one provided several conditions are met:

1. the ratio of the superlattice cell size to the characteristic scale length of the small hydrodynamics fluctuation is close to zero, $\frac{\ell_s}{L} \sim 0$ (satisfied in the continuum limit)

2. the angular distribution of particles along momentum directions is close to an isotropic one

3. the flow is subsonic (M $\ll 1$)

4. spatial gradients are small (Kn ~ 0 and $\frac{\delta\rho}{\rho}$ is small).

2.2.3 Derivation of the Continuum Equations

The local mass density and the momentum density at $\vec{x}$ and t can be expressed in terms of the occupancy probability, $f_a(\vec{x},t)$, is

$$\rho(\vec{x},t) = \lim_{\ell_s \to 0} \sum_{a=1}^{B} m\ f_a(\vec{x},t) \tag{2.34}$$

$$\rho(\vec{x},t) v_i(\vec{x},t) = \lim_{\ell_s \to 0} \sum_{a=1}^{B} mc^2 e_{ai}\ f_a(\vec{x},t). \tag{2.35}$$

The mass and momentum densities are considered "macroscopic" field quantities. They are only well defined in the *continuum limit*, where the primitive cell size of the lattice approaches zero. However, for practical considerations, they are approximated by high resolution grids with small but finite cell size.

The derivation of the continuum equations of motion at the macroscopic scale is carried out in this section. The method of derivation is outlined by these following few steps:

1. Expand the mesoscopic Boltzmann equation to first order in time and second order in space.[5]
2. In the continuum limit, calculate the first and second moments of the mesoscopic Boltzmann equation .[6]
3. Insert the mesoscopic occupancy probability given Equation (2.33) into the moment equations obtained in Step 2.

After some algebraic manipulations, we thereby obtain an approximation of the equations of motion that serve as an effective field theory at the macroscopic scale. Because of diffusive ordering, the result is that the macroscopic equations of motion are a set of coupled parabolic partial differential equations. In the present derivation, I do not give a multi-scale analysis such as the one carried out by Frisch *et al.* [3] in their treatment of 2 and 3 dimensional lattice-gas hydrodynamics. This omission is justified because only a single time-scale is needed for most lattice-gas systems since the transport coefficients are very large. That is, there is little or no separation between the short time scale associated with sound mode excitations and the longer time scale associated with viscous mode excitations arising from momentum diffusion. Viscous damping in lattice-gas fluids is observed over relatively short-time scales and therefore significantly affects, and is mixed in with, sound wave propagation and convection. Nevertheless, at the end of this section, I will divide the effective field theory into two sets of equations that apply at short and long time scales.

We determine the macroscopic equations of motion using the lattice Boltzmann equation

$$\frac{df_a}{dt} = \lim_{\substack{\tau \to 0 \\ \ell_s \to 0}} \frac{\Omega_a^{\text{meso}}}{\tau}. \tag{2.36}$$

In consideration of diffusive ordering, we expand the L.H.S. of this equation to first-order in time and second-order in space

$$\frac{\partial f_a}{\partial t} + c\hat{e}_a \cdot \nabla f_a + \frac{\ell_s^2}{2\tau}(\hat{e}_a \cdot \nabla)^2 f_a + \mathcal{O}(\text{Kn}^3, \text{Sh}^2) = \lim_{\substack{\tau \to 0 \\ \ell_s \to 0}} \frac{\Omega_a^{\text{meso}}}{\tau}. \tag{2.37}$$

[5] Only a first order time derivative is needed because of the long-time scales associated with viscous damping. Time and spatial scales are related parabolically ($T \sim L^2$ or $\varepsilon^2 \sim \delta x^2 \sim \delta t$) in lattice-gas systems.

[6] This is done because for each additive conserved quantity of the dynamics, a macroscopic field is expressed as a moment of the mesoscopic field of probability of occupancies. In the present case, ρ and $\vec{v}$ are expressed in terms of the f_a's according Equations (2.34) and (2.35).

This is called the *lattice-Boltzmann equation*, where Ω_a^{meso} is defined by Equation (2.5). Since $\sum_a \Omega_a^{\text{meso}} = 0$, the zeroth moment of Equation (2.37) is

$$\partial_t \left(m \sum_a f_a \right) + \partial_i \left(mc \sum_a e_{ai} f_a \right) + \frac{\ell_s^2}{2\tau} \partial_i \partial_j \left(\sum_a e_{ai} e_{aj} f_a \right) + \mathcal{O}(\text{Kn}^3, \text{Sh}^2) = 0. \tag{2.38}$$

Using the identities [1]

$$\sum_{a=1}^{B} \hat{e}_a = 0 \tag{2.39}$$

$$\sum_{a=1}^{B} \hat{e}_a \hat{e}_a = \frac{B}{D} \Delta^{(2)} \tag{2.40}$$

$$\sum_{a=1}^{B} \hat{e}_a \hat{e}_a \hat{e}_a = 0 \tag{2.41}$$

$$\sum_{a=1}^{B} \hat{e}_a \hat{e}_a \hat{e}_a \hat{e}_a = \frac{B}{D(D+2)} \Delta^{(4)}, \tag{2.42}$$

the corrected occupancy probability Equation (2.33), along with definitions for the mass density Equation (2.34) and momentum density Equation (2.35), this reduces to a mass continuity equation in the long-wavelength, low-frequency, and subsonic limits

$$\partial_t \rho + \partial_i (\rho v_i) + \mathcal{O}(\text{Kn}^3, \text{Sh}^2, \text{M}^3) = 0. \tag{2.43}$$

Since $\sum_a e_{ai} \Omega_a^{\text{meso}} = 0$ too, the first moment of Equation (2.37) is

$$\partial_t \left(mc \sum_a e_{ai} f_a \right) + \partial_j \left(mc^2 \sum_a e_{ai} e_{aj} f_a \right) + \frac{\ell_s^2}{2\tau} \partial_j \partial_k \left(mc \sum_a e_{ai} e_{aj} e_{ak} f_a \right) + \mathcal{O}(\text{Kn}^3, \text{Sh}^2) = 0. \tag{2.44}$$

This reduces to Euler's equation in the long-wavelength, low-frequency, and subsonic limits

$$\partial_t (\rho v_i) + \partial_j \Pi_{ij} + \mathcal{O}(\text{Kn}^3, \text{Sh}^2, \text{M}^3) = 0, \tag{2.45}$$

where the momentum flux density is

$$\Pi_{ij} = P_{ij} + g \rho v_i v_j - \frac{\rho \ell_s^2}{(D+2)\tau \kappa_\eta} \partial_j v_i + \frac{\ell_s^2}{2\tau} \frac{\rho}{(D+2)} \partial_j v_i \tag{2.46}$$

or

$$\Pi_{ij} = P_{ij} + g \rho v_i v_j - \frac{\rho \ell_s^2}{(D+2)\tau} \left(\frac{1}{\kappa_\eta} - \frac{1}{2} \right) \partial_j v_i. \tag{2.47}$$

The shift of $-\frac{1}{2}$ is a constant negative contribution to the shear viscosity by a lattice effect. With sound speed $c_s \equiv \frac{\ell_s}{\tau \sqrt{D}}$, identify the isotropic pressure tensor as

$$P_{ij} = \rho c_s^2 \left(1 - g \frac{v^2}{c^2} \frac{\ell^2}{\ell_s^2} \right) \delta_{ij}. \tag{2.48}$$

Finally, inserting Equation (2.47) into Euler's equation Equation (2.45), the momentum equation for viscous flow is

$$\partial_t (\rho v_i) + \partial_j (g \rho v_i v_j) + \mathcal{O}(\text{Kn}^3, \text{Sh}^2, \text{M}^3) = -\partial_i P + \eta \partial^2 v_i + \left(\zeta + \frac{\eta}{D} \right) \partial_i \partial_j v_j, \tag{2.49}$$

with shear viscosity

$$\eta = \frac{\rho \ell_s^2}{\tau} \frac{1}{D+2} \left(\frac{1}{\kappa_\eta} - \frac{1}{2} \right), \tag{2.50}$$

and bulk viscosity

$$\zeta = \frac{\rho \ell_s^2}{\tau} \frac{2D-1}{D(D+2)} \left(\frac{1}{\kappa_\eta} - \frac{1}{2} \right). \tag{2.51}$$

With small Knudsen, Strouhal, and Mach numbers, the momentum equation Equation (2.49) approximates the Navier-Stokes equation except that there is an extra density-dependent factor, $g(d)$, in the convective term in Equation (2.49). If g is not unity, Galilean invariance is destroyed. It is possible to alter the collision term in the lattice Boltzmann equation so that $g = 1$. This was first done by H. Chen, S. Chen, and Mattaeus [59], but their approach violated detailed balance, and consequently the algorthm is subject to unphysical numerical instabilities. Unconditionally numerically stable lattice-gas methods that obey the principle of detailed balance have also been found to set $g = 1$ [5, 39].

For lattice-gas systems with low viscosity [102], it is appropriate to consider two separate effective field theories for short-time and long-time hydrodynamic behavior. The short and long hydrodynamic time scales are denoted by t_1 and t_2, respectively. A multi-scale formalism is used where $\partial_t \longrightarrow \partial_{t_1} + \partial_{t_2}$ [3]. Then the effective field theory defined by the continuity equation Equation (2.43) and the Navier-Stokes equation Equation (2.45) reduces at the short-time hydrodynamic scale to the following set

$$\partial_{t_1} \rho + \partial_i (\rho v_i) = 0 \tag{2.52}$$

$$\partial_{t_1} (\rho v_i) = -\partial_j P. \tag{2.53}$$

This set models sound wave propagation induced by pressure gradients in a compressible fluid. At the long-time hydrodynamics scale, Equations (2.43) and (2.45) reduce to

$$\partial_{t_2} \rho = 0 \tag{2.54}$$

$$\partial_{t_2} (\rho v_i) + \partial_j (g \rho v_i v_j) = \eta \partial^2 v_i + \left(\zeta + \frac{\eta}{D} \right) \partial_i \partial_j v_j. \tag{2.55}$$

This set of equations describes viscous damping and convection for a compressible fluid.

Chapter 3

A One-Dimensional Model with Conserved Mass and Momentum

3.1 Microscopic Rules

Let us consider the simplest lattice-gas model of a one-dimensional fluid with two conserved quantities. This is called the *1D3Px lattice-gas model*. This model was first studied by Qian in 1990 [103]. The lattice gas is one dimensional and has three bits per site, a rest particle with mass two and speed ± 1 particles with mass one. The mass and momentum at a lattice site is

$$m = 2n_0 + n_1 + n_2 \qquad \text{and} \qquad p_x = n_1 - n_2. \tag{3.1}$$

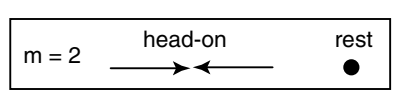

Figure 3.1: Head-on collision in the 1D3Px lattice-gas model. The single equivalence class has $m = 2$ and $p_x = 0$.

There are two local configurations both with $m = 2$ and $p_x = 0$: (1) $\{n_0, n_1, n_2\} = \{1, 0, 0\}$ and (2) $\{n_0, n_1, n_2\} = \{0, 1, 1\}$. These two configurations are members of the only collision set (which is called an *equivalence class*). An equivalence class has two or more members. Figure 3.1 illustrates the equivalence class of the 1D3Px model. Its two elements are the configuration of two head-on particles $\{011\}$ and the configuration with a single rest particle $\{100\}$.

Because the total number of particles and the total momentum must be conserved, the collision part of the dynamics can only permute the local configurations. The collision equation, which is applied homogeneously across the lattice, can be expressed in terms of a mapping function, U, as follows

$$s' = U(s), \tag{3.2}$$

where U maps 2^B configurations to 2^B new configurations. For the simple 1D3Px lattice, U is

$$\begin{aligned} U(\{011\}) &= \{100\} \\ U(\{100\}) &= \{011\}. \end{aligned}$$

If a configuration s is not a member of an equivalence class, then $U(s) = s$. In other words, if the incoming state is not a member of an equivalence class, then the outgoing state is set equal to the incoming state. To speed up a lattice-gas simulation, the mapping function, U, may be precomputed before the simulation and accessed in *lookup table* fashion during the simulation.

In a computer implementation, it is convenient to use two arrays to simultaneously store the states s and s'. Therefore, in Equation (3.2), data in the array that stores the "incoming" state, s, is transformed by the action of the lookup table U (which is applied homogeneously over the entire array) and the output is written into the next array to store the new "outgoing" state, s'.

It is conventional to write the collision rule in terms of the occupation variables, $n_a = 1$ or 0, which are Boolean values. The collision rule, expressed for an individual local state, is written

$$n'_a(\vec{x}, t) = n_a(\vec{x}, t) + \Omega_a(n_*), \tag{3.3}$$

where the collision term $\Omega_a(n_*) = \pm 1$ or 0. Writing $\Omega_a(n_*)$ with an asterisk subscript on n_* denotes that the collision term for the ath local state depends on all the on-site local states. It is conventional to write the streaming rule in terms of n_a also

$$n_a(\vec{x} + \ell\hat{e}_a, t + \tau) = n'_a(\vec{x}, t). \tag{3.4}$$

Combining Equations (3.3) and (3.4), the *microscopic transport equation* is therefore

$$n_a(\vec{x} + \ell\hat{e}_a, t + \tau) = n_a(\vec{x}, t) + \Omega_a(n_*). \tag{3.5}$$

For the 1D3Px model, the lattice vectors are $\hat{e}_0 = \vec{0}$, $\hat{e}_1 = \hat{x}$, and $\hat{e}_2 = -\hat{x}$, and the collision term is specified by the single function

$$\Omega = n_1\ n_2\ (1 - n_0) - n_0\ (1 - n_1)(1 - n_2). \tag{3.6}$$

where $\Omega_0 = \Omega$, and $\Omega_{1,2} = -\Omega$. Then explicitly for the 1D3Px model, the microscopic transport equation Equation (3.5) is

$$\begin{aligned} n_0(x, t + \tau) &= n_0(x, t) + \Omega(x, t) \\ n_{1,2}(x \pm \ell, t + \tau) &= n_{1,2}(x, t) - \Omega(x, t). \end{aligned} \tag{3.7}$$

Successive snap shots of the microscopic time evolution of a small classical lattice-gas system on a one-dimensional linear grid with 1024 sites is shown in Figure 3.2. The particles (which look like lines on a barcode) are rendered in black on the right side of the diagram. Each cell comprises 3 local states and hence each cell can hold up to 3 particles. Bit 0 encodes the $m = 2$ "rest" particle state, and bits 1 and 2 encodes states with $m = 1$ particles moving with speed +1 and -1, respectively. Initially, at $t = 0$, most of the particles reside on the left half of the lattice and successive snapshots are shown at every 128 time steps. A spatial coarse-grain average, with block size of 128, is used to determine the "mass density field"; the total mass per site is plotted on the left side of the figure. The initial state, rendered in red, is a sinusoidal perturbation with a background density of $\rho = \frac{1}{4}$ and an amplitude of $\delta\rho = \frac{1}{5}$. (The magnitude of $\delta\rho$ is exaggerated here for pedagogical purposes; it is usually a few percent of the background density.) At $t = 640$, the situation is reversed as most of the particles have moved to local states on the right half of the lattice. The final mass density waveform is rendered in blue. Each microscopic configuration of particles rendered in this figure corresponds to a unique state of the lattice-gas system. Even though this is a small system with only 1024 lattice sites, the total number of unique states available is still an extremely large number, 2^{3072}. The sound speed is clearly less than unity, because for the wave to move halfway cross the grid, 512 lattice units, it takes over 640 time steps.

3.2 Model Analysis

A lattice Boltzmann equation describes the dynamics of the 1D3Px lattice-gas system at the mesoscopic scale. The mesoscopic average of the occupation variable, $n_a(\vec{x}, t)$, is the probability of occupancy

$$f_a(\vec{x}, t) \equiv \langle n_a(\vec{x}, t) \rangle. \tag{3.8}$$

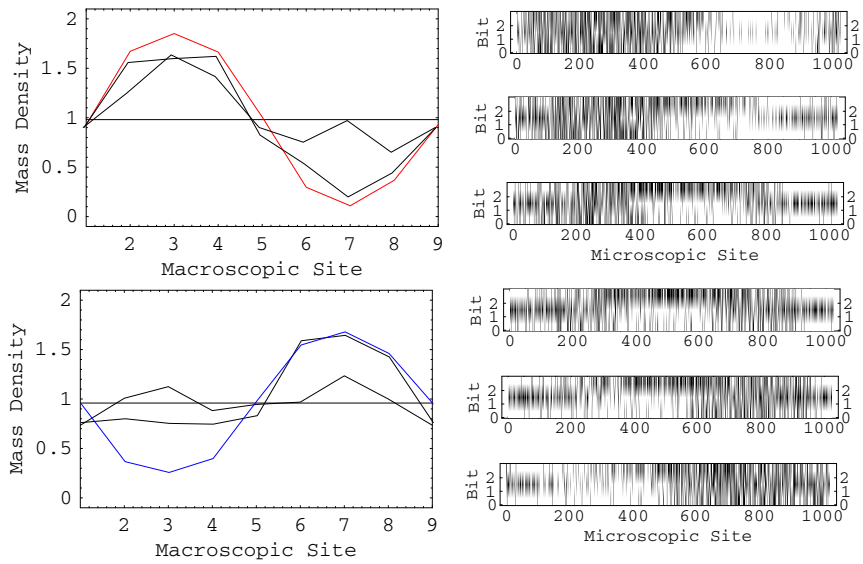

Figure 3.2: Successive snapshots of the microscopic state of a classical 1D3Px lattice-gas system with a small grid of $V = 1024\ell$ sites. The six plots on the right show the individual particle occupancies of the microscopic state at time step intervals of 128τ. The three local states per site of the 1D3Px model are plotted in the vertical, respectively labeled bits 0, 1, and 2. A black line marked on a local state indicates that that local state is occupied by a single particle. The profiles on the left show the mass density obtained by coarse-grain averaging over blocks of 128 microscopic cells (*i.e.* total mass of all particles in a block divided by the block size). On the upper left plot, the red sinusoid is the initial profile at $t = 0\tau$ and subsequent profiles at $t = 128\tau$ and $t = 256\tau$ are overplotted. On the lower left plot, the profiles at $t = 384, 512$, and 640τ are shown. The final sinusoid occurring at $t = 640\tau$ is rendered in blue.

Here, the angled brackets around a microscopic quantity denote its mesoscopic expectation value obtained by ensemble averaging. The kinetic transport equations are

$$\begin{aligned} f_0(x, t+\tau) &= f_0(x,t) + \langle \Omega(x,t) \rangle \\ f_{1,2}(x \pm \ell, t+\tau) &= f_{1,2}(x,t) - \langle \Omega(x,t) \rangle. \end{aligned} \tag{3.9}$$

To carry out a classical lattice-gas simulation at the mesoscopic scale, we can approximate $\Omega^{\rm meso}(x,t) \equiv \langle \Omega(x,t) \rangle$ by a *mean-field* collision term, denoted $\Omega^{\rm mf}(x,t)$, that neglect particle-particle correlations

$$\langle \Omega(x,t) \rangle \simeq \Omega^{\rm mf}(x,t) = f_1\ f_2\ (1-f_0) - f_0\ (1-f_1)(1-f_2). \tag{3.10}$$

A statement of detailed balance can be written by setting the mean-field value of the collision term, Equation (3.10), to zero at equilibrium

$$\langle \Omega \rangle \simeq \Omega^{\rm mf}(f_*^{\rm eq}) = 0. \tag{3.11}$$

Therefore, the probability of occupancies satisfies the following equation

$$f_0^{\rm eq} = \frac{f_1^{\rm eq} f_2^{\rm eq}}{f_1^{\rm eq} f_2^{\rm eq} + (1-f_1^{\rm eq})(1-f_2^{\rm eq})}. \tag{3.12}$$

This equation, along with equations for the mass and momentum densities

$$\rho_\circ = 2 f_0^{\rm eq} + f_1^{\rm eq} + f_2^{\rm eq} \qquad \text{and} \qquad u_{x\circ} = f_1^{\rm eq} - f_2^{\rm eq}, \tag{3.13}$$

gives us a nonlinear system of three equations in five unknowns, $f_0^{\rm eq}$, $f_1^{\rm eq}$, $f_2^{\rm eq}$, $\rho_\circ$, and $u_{x\circ}$. Hence, it is possible to analytically solve for the occupation probabilities, $f_0^{\rm eq}$, $f_1^{\rm eq}$, and $f_2^{\rm eq}$, in terms of $\rho_\circ$ and

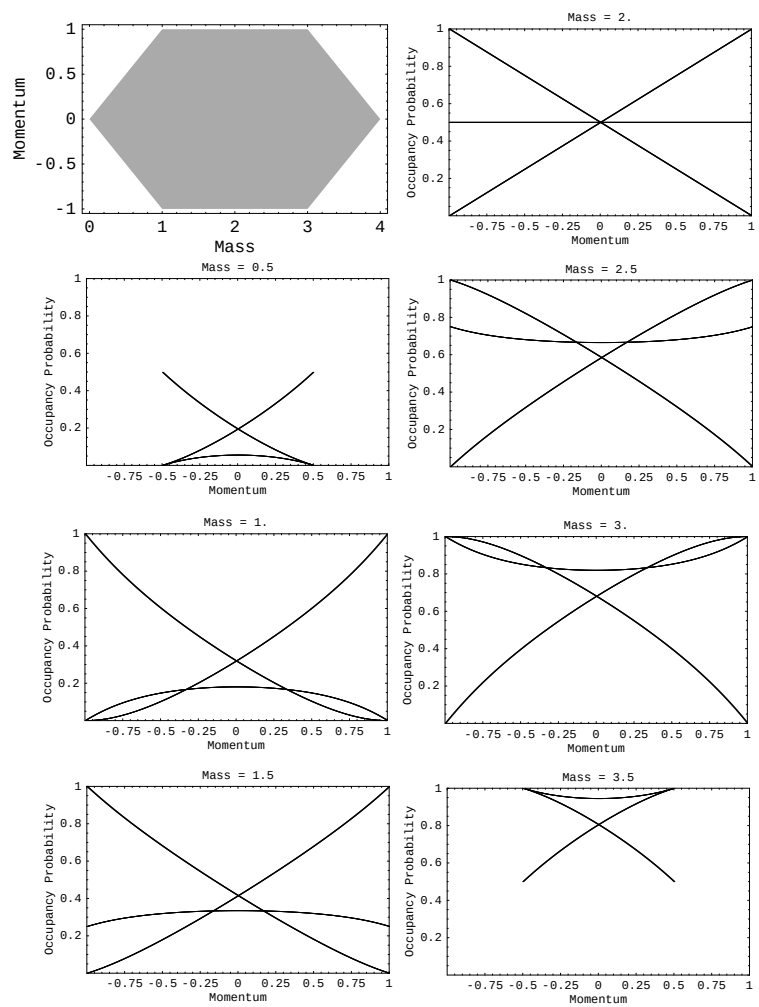

Figure 3.3: A *bounding polytope* for the 1D3Px lattice gas is plotted in the upper left corner (here the mass on the x-axis is in units of the individual particle mass, denoted m). The other plots are the computed equilibrium probability occupancies. The units for momentum on all the plots are $m\frac{\ell}{\tau}$.

$u_{x\circ}$. The resulting functions are plotted in Figure 3.3. The shaded region region in the upper left plot gives the allowable values for mass and momentum for the 1D3Px lattice-model. The equilibrium probability of occupancy of the rest particle, $f_0^{\rm eq}$, and the speed ± 1 moving particle states, $f_1^{\rm eq}$ and $f_2^{\rm eq}$, can be analytically determined for the 1D3Px model. The results are plotted for a range of masses from $m = 0.5$ up to $m = 3.5$. The particle-hole symmetry about half-filling ($m = 2$) of this lattice-gas model is apparent in Figure 3.3 (for example, the $m = 0.5$ plot is identically inverted from the $m = 3.5$ plot). $f_0^{\rm eq}$ is concave downward below half-filling and concave upward above half-filling. Furthermore, below half-filling, $f_1^{\rm eq}$ monotonically increases with increasing momentum while $f_2^{\rm eq}$ monotonically decreases. The situation is reversed above half-filling, as expected.

When the system is at rest at equilibrium, $p_x = 0$, then $f_1^{\rm eq} = f_2^{\rm eq} = d$ and the probability of occupancy for the rest particle state is

$$f_0^{\rm eq} = \frac{d^2}{1 - 2d + 2d^2}. \tag{3.14}$$

Using Equation (3.10), then the Jacobian of the collision, $J_{ab} \equiv \left.\frac{\partial \Omega_a^{\rm mf}}{\partial f_b}\right|_{f^{\rm eq}}$, is

$$J = \begin{pmatrix} -1 + 2d - 2d^2 & \frac{(1-d)d}{1-2d+2d^2} & \frac{(1-d)d}{1-2d+2d^2} \\ 1 - 2d + 2d^2 & \frac{(d-1)d}{1-2d+2d^2} & \frac{(d-1)d}{1-2d+2d^2} \\ 1 - 2d + 2d^2 & \frac{(d-1)d}{1-2d+2d^2} & \frac{(d-1)d}{1-2d+2d^2} \end{pmatrix} \tag{3.15}$$

The eigenvectors of J are

$$|1\rangle = (2, 1, 1) \tag{3.16}$$
$$|2\rangle = (0, 1, -1) \tag{3.17}$$
$$|3\rangle = \left(\frac{(1 - 2d + 2d^2)^2}{d(d-1)}, 1, 1\right). \tag{3.18}$$

The eigenvectors $|1\rangle$ and $|2\rangle$, corresponding to mass and momentum, span a two-dimensional hydrodynamic subspace. The remaining eigenvector, $|3\rangle$, is a kinetic eigenvector, which in this case is density dependent. The eigenvalues of J are

$$\lambda_1 = 0 \tag{3.19}$$
$$\lambda_2 = 0 \tag{3.20}$$
$$\lambda_3 = \frac{1 - 2d + 6d^2 - 8d^3 + 4d^4}{-1 + 2d - 2d^2}. \tag{3.21}$$

Now using the lattice vectors, $\hat{e}_0 = 0$, $\hat{e}_1 = 1$, and $\hat{e}_2 = -1$, and the expression for J given in Equation (3.15), setting the determinant the linearized lattice-Boltzmann equation equal to zero

$$\left|\left(e^{i(\ell_s \hat{e}_a \cdot \vec{k} + \omega\tau)} - 1\right)\mathbf{1} - J\right| = 0 \tag{3.22}$$

allows us to solve to the dispersion relations for the system. Taking $\ell = \tau = 1$, we get the following dispersion relation

$$(1 - 2d + 2d^2)e^{3\omega} - 2[d - 3d^2 + 4d^3 - 2d^4 + (1 - 3d + 3d^2)\cos k]e^{2\omega} + \tag{3.23}$$
$$(1 - 2d)^2[1 + 2d(d-1)\cos k]e^{\omega} + 4d^2(d-1)^2 = 0. \tag{3.24}$$

This is a cubic equation in e^{ω}, and it is analytically solvable. The only hydrodynamic mode is a damped sound wave, as expected. Plots of the dispersion relation for various background densities are given in Figure 3.4.

Real and imaginary parts of the dispersion relations for the 1D3Px lattice-gas model, shown respectively on the left and right hand sides of the Figure 3.4. The real part of the dispersion

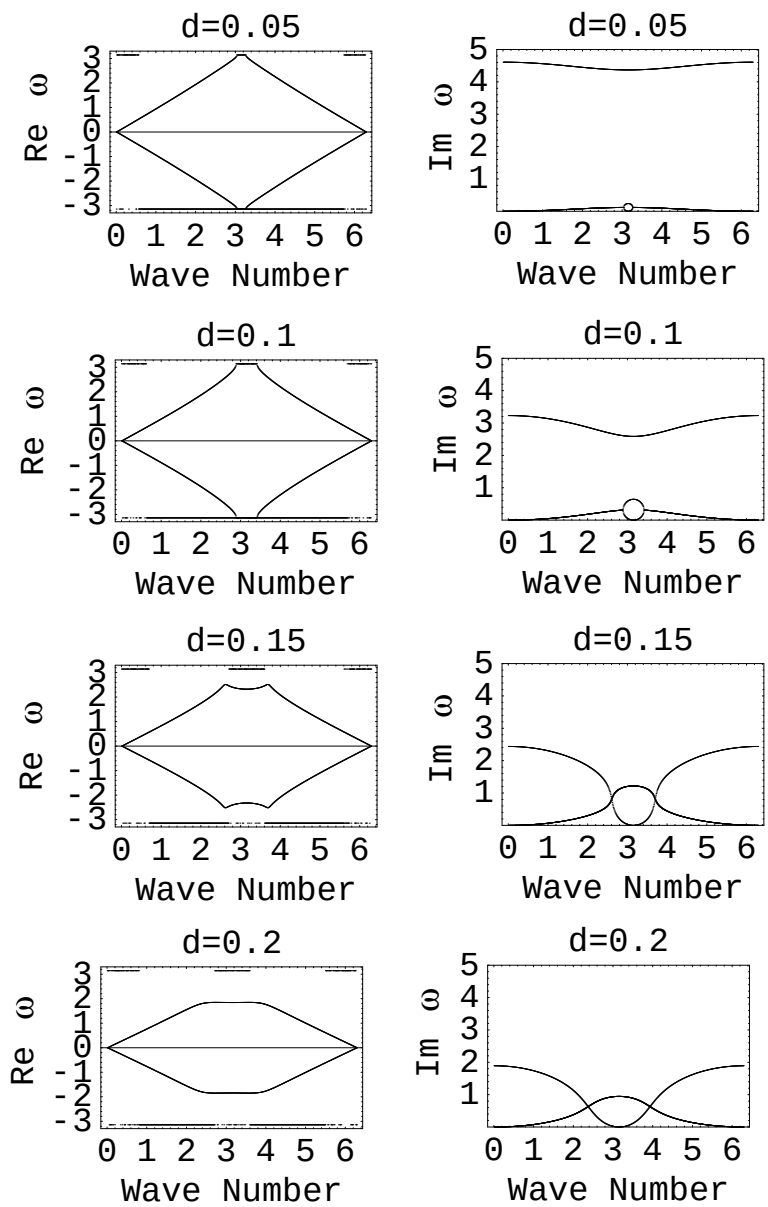

Figure 3.4: The real and imaginary parts of the dispersion relations for the 1D3Px lattice gas for a range of background densities from $d = 0.05$ to $d = 0.2$.

relations indicates a sound mode ($\Re(\omega) \to \pm c_s k$ as $k \to 0$). The imaginary part of the dispersion relation for the hydrodynamic mode is parabolic for small wavenumber, indicating viscous damping of the sound mode ($\Im(\omega) \to \Gamma k^2$ as $k \to 0$). Remarkably, the sound damping constant, Γ, approaches zero as the background mass density approaches zero. That is, low-mass density waves can oscillate without viscous damping. This behavior is observed in numerical simulations of the 1D3Px model.

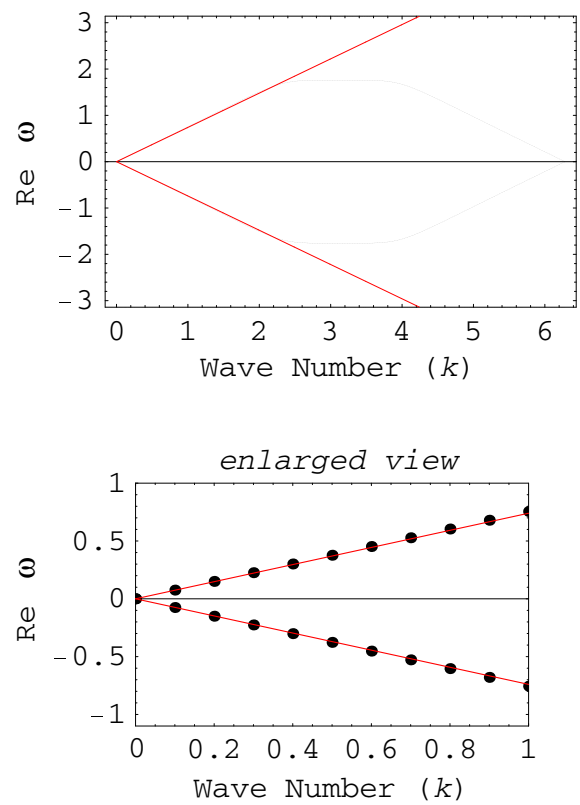

Figure 3.5: Real part of the dispersion relation for the mesoscopic 1D3Px lattice gas in the long wavelength limit and mean-field limit at a reduced background density of $d = 0.214286$.

The real part of the dispersion relation for the sound mode for the 1D3Px lattice-gas model set with a background density of $d = \frac{6}{4V}$, with $V = 7$, is shown in Figure 3.5. The real part of the dispersion relation indicates a sound mode ($\Re(\omega) \to \pm c_s k$ as $k \to 0$ where $c_s = 0.74\frac{\ell}{\tau}$). The data points, plotted as black circles, are solutions to the linearized Boltzmann equation in the mean-field limit. The solid red curves, with slope of $\pm c_s$, are numerical linear fits to the data. The imaginary part of the dispersion relation for the sound mode for the 1D3Px lattice-gas model is shown in Figure 3.6. The imaginary part of the dispersion relation indicates sound damping ($\Im(\omega) \to i\Gamma k^2$ as $k \to 0$ where $\Gamma = 0.08\frac{\ell^2}{\tau}$. The solid red parabola is a numerical fit to the data in the region of small $k < 1$. The calculations shown in Figures 3.5 and 3.6 were done with a mass density filling fraction of $d_\circ = \frac{6}{4V} = 0.214$, where a small system size of $V = 7$ is used. In this case, $k = \frac{2\pi}{V} = 0.898$.

3.3 Comparing Analytical and Numerical Predictions

A time history of the mass density wave for a small system with $V = 7$ sites is shown in Figure 3.7. The exponential envelope over plotted in red analytically determined by an analysis of the linearized lattice Boltzmann equation in the mean-field limit (see Figure 3.6). The predicted sound damping

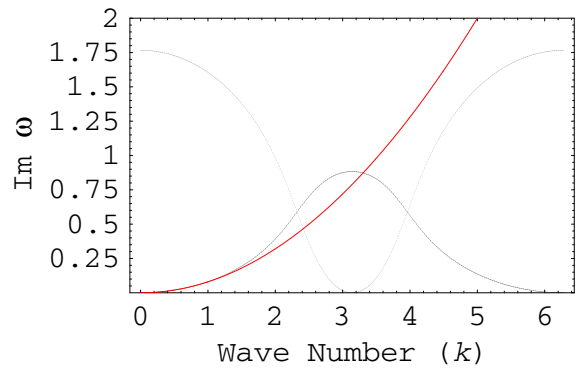

Figure 3.6: The imaginary part of the dispersion relation for the mesoscopic 1D3Px lattice gas in the long wavelength limit and mean-field limit at a reduced background density of $d = 0.214286$.

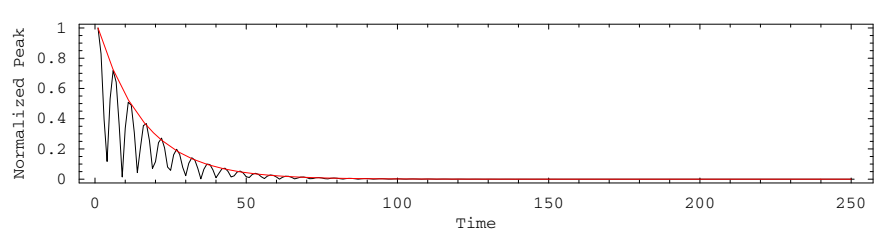

Figure 3.7: Damping of a mass density wave for a system with $V - 7$ sites in the classical 1D3Px model simulated using a mesoscopic Boltzmann equation with the collision term expressed in the mean-field approximation. The background density is $d_\circ = \frac{6}{4V} = 0.214$. The ordinate is the absolute value of the amplitude of mass-density wave divided by the peak amplitude of the initial perturbation.

constant, $\Gamma = 0.08\frac{\ell^2}{\tau}$ is in excellent agreement with the simulation data.

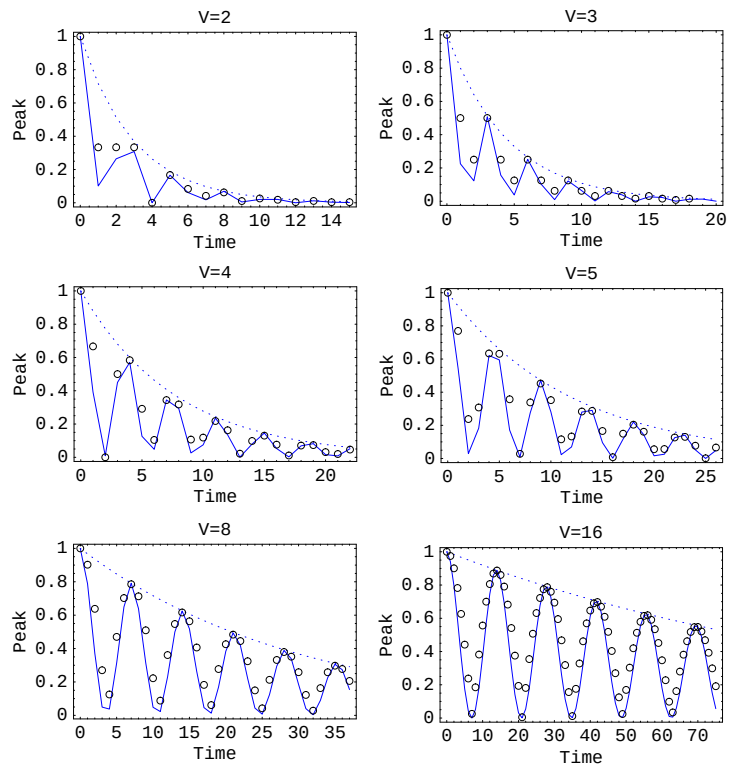

Figure 3.8: Damping of a mass density wave at multiple scales in the classical 1D3Px model simulated using a mesoscopic Boltzmann equation with the collision term expressed in the mean-field approximation. The abscissa is plotted in units of τ and the ordinate is plotted as the absolute value of the amplitude of mass-density wave divided by the peak amplitude of the initial perturbation.

Damping of mass density waves in the classical 1D3Px lattice gas for different system sizes, $V = 2, 3, 4, 5, 8$ and 16 is shown in Figure 3.8. The simulation is initialized with a sinusoidal perturbation of $\delta\rho = 0.04$ from a uniform background mass density at half-filling, $\rho = 2$. So the fractional mass density variation is initially one part in fifty. The wavelength equals the system size. Plotted is the time history of the resulting standing wave. The peak amplitude decays in time because of viscous damping. The circles are data taken from classical mesoscopic simulations, using a mean-field collision operator. The solid blue curve is a nonlinear numerical fit to the data using an exponentially damped sinusoid $e^{-\frac{t}{\tau}} \cos \omega t$ with free parameters for the angular frequency, ω, and the damping constant, τ. The dotted blue curve is the envelope of the damped curve. For system sizes as small as $V = 3$, the oscillations are clearly apparent. Even in the smallest possible system only with two sites, $V = 2$, oscillations are discernable, and the data agrees with an exponentially damped sinusoid. This is an example of "fluid-like" behavior occurring in systems far below from the continuum limit.

Plotted in Figure 3.9 is damping time constants of mass density waves in the classical 1D3Px lattice gas for different system sizes from $V = 2$ up to $V = 256$. The log-log plot shows the power-law behavior, known as *diffusive ordering*, typical of lattice-gas system in the viscous regime. The power law in this case is $T = 0.44V^2$, which is parabolic. Each circle is determined from a mesoscopic scale simulation that initialized with a sinusoidal perturbation of $\delta\rho = 0.04$ from a uniform background mass density at half-filling, $\rho = 2$. The damping constant, $\Gamma = \frac{\ell^2}{T}$, is determined from the envelope of the resulting standing wave $e^{-\frac{t}{T}} \cos \omega t$ (see Figure 3.8). The mean-field estimates of the damping time constant are the circles. The solid blue line is a linear best fit to these estimates. The estimated

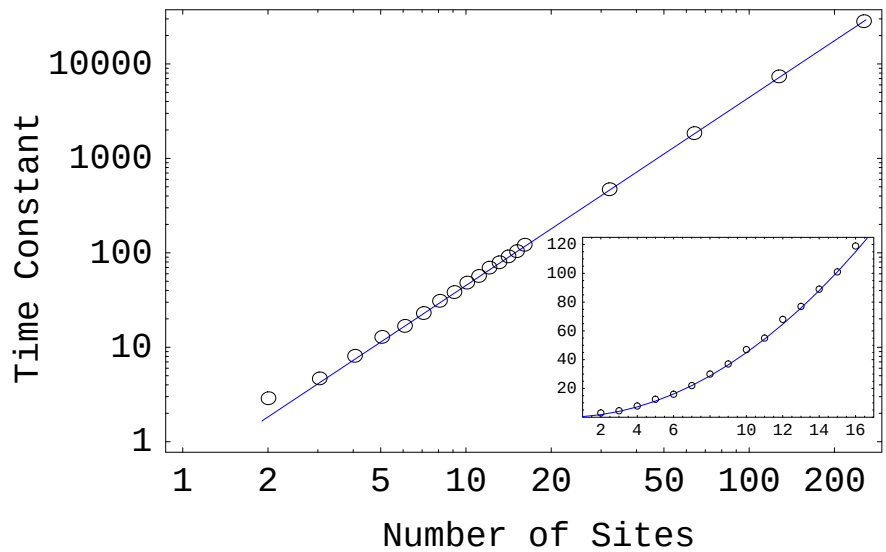

Figure 3.9: Diffusive ordering in the classical 1D3Px model computing at the mesoscopic scale using the mean-field approximation.

damping constant deviates only slightly from power-law behavior at the smallest system sizes. The inset plot is a linear plot of the data for $V \leq 16$ and the solid-blue parabola is the same diffusive-ordering power-law in the larger log-log plot.

Chapter 4

A Two-Dimensional Model with Conserved Mass and Momentum

4.1 Microscopic Rules

In the two-dimensional lattice gas on a triangular lattice ($B = 6$) there are 9 equivalence classes:

- a three member equivalence class for the 2-body head-on collisions $\vec{p} = 0$;
- a two member equivalence class for the symmetric 3-body collisions with $\vec{p} = 0$;
- six two member equivalence classes for 2-body head-on collisions with a spectator particle (or 3-body asymmetric collisions) with momentum $\vec{p} = mc\hat{e}_a$; and, finally,
- a three member equivalence class for the 4-body collision with $\vec{p} = 0$, which is the particle-hole counterpart of the 2-body equivalence class.

The equivalence classes are illustrated in Figure 4.1. The first two are the equivalence classes used in the FHP model [2]. There are three conserved quantities for this two-dimensional system: the mass, and two components of the momentum.[1] Energy is also conserved, but this is degenerate with the mass since the particles move at unit speed. The FHP model does not use the other 7 equivalence classes, even though adding them in takes no extra computational or analytical work.

Let the incoming configuration at a spacetime coordinate $(\vec{x}, t)$ be denoted by the set $s(\vec{x}, t) = \{n_1(\vec{x}, t), n_2(\vec{x}, t), \ldots, n_B(\vec{x}, t)\}$. After the collision step, the outgoing configuration is denoted $s'(\vec{x}, t) = \{n'_1(\vec{x}, t), n'_2(\vec{x}, t), \ldots, n'_B(\vec{x}, t)\}$. Taking $B = 6$ for example, a 3-body collision can have an incoming configuration

$$\{1\ 0\ 1\ 0\ 1\ 0\}$$

and an outgoing configuration

$$\{0\ 1\ 0\ 1\ 0\ 1\},$$

or vice versa. In the case of a 2-body collision, if the incoming configuration is

$$\{1\ 0\ 0\ 1\ 0\ 0\},$$

then the outgoing configuration could be either

$$\{0\ 1\ 0\ 0\ 1\ 0\} \qquad \text{or} \qquad \{0\ 0\ 1\ 0\ 0\ 1\}.$$

[1] If we use only the 2-body collisions in Figure 4.1, then there is would be additional conserved quantity (the difference in the particle number along each of the three lattice directions give three conserved momenta instead of two). So there would be a *spurious invariant*. Consequently, the symmetric 3-body collisions in Figure 4.1 are needed in the FHP-model to remove this spurious invariant [2].

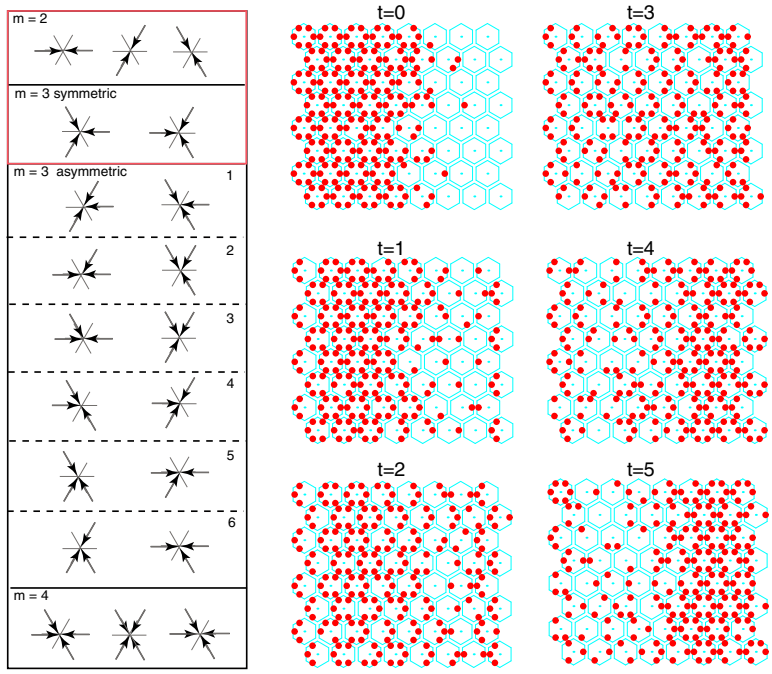

Figure 4.1: Successive snap shots of the time evolution of a small classical lattice-gas system on a two-dimensional 8×8 triangular grid. The particles are rendered in red and the underlying hexagonal cells of the Bravais lattice are rendered in blue. Each hexagonal cell comprises 6 local states and hence each cell can hold up to 6 particles. There are nine collision sets, called *equivalence classes*. The first three head-on $m = 2$ collisions and two symmetric $m = 3$ collisions, shown in the red box, constitute the *FHP lattice-gas model*. (Viscous dissipation can be reduced if the $m = 3$ asymmetric collisions and the $m = 4$ collisions are used, but they are not necessary.) Initially, at $t = 0$, most of the particles reside on the left half of the lattice. (The sinusoidal profile across the lattice is highly exaggerated for display purposes, so the system is very far from local equilibrium.) After a few time steps, at $t = 5$, the situation is reversed as most of the particles have moved to local states on the right half of the lattice. Each configuration of particles rendered in this figure corresponds to a unique state of the lattice-gas system. Even though this is a small system with only 64 lattice sites, the total number of unique states available is still a rather large number, 2^{384}. The CAM-8, our fastest lattice-gas computer, which can update 25 million sites per second, would have to run for over 10^{100} years to enumerate every possible state of this small 8×8 example.

The collision part of the classical dynamics permutes the particles locally because the total number of particles and the total momentum must be conserved. The collision equation, which is applied homogeneously across the lattice, is the following

$$s' = U(s),$$

where U is a 64 element *lookup table* defined by

$$\begin{aligned}
U(\{100100\}) &= \alpha\{010010\} + (1-\alpha)\{001001\} \\
U(\{010010\}) &= \alpha\{001001\} + (1-\alpha)\{100100\} \\
U(\{001001\}) &= \alpha\{100100\} + (1-\alpha)\{010010\} \\
U(\{101010\}) &= \{010101\} \\
U(\{010010\}) &= \{101010\},
\end{aligned}$$

where the $\alpha \in \{0,1\}$ is chosen uniformly randomly. If a configuration s is not a member of the either the 2-body or the 3-body FHP equivalence classes, then $U(s) = s$. In other words, if the incoming state is not a member of an equivalence class, which has two or more members, then the outgoing state is set equal to the incoming state. Some fluid simulation examples of the FHP model are shown in Figures 4.2 and 4.3.

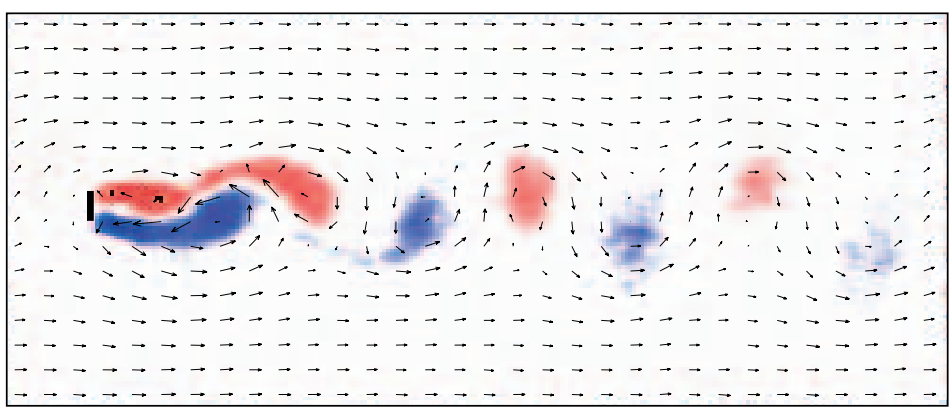

Figure 4.2: Classical lattice gas fluid simulation with a lattice size of 4096×2048 done on the CAM-8 using about 10 million particles. Momentum and vorticity fields display a Von Karman Street. Coarse-gain averaging was done over 50 time steps, using a 64×64 spatial block size for the momentum field, and a 16×16 spatial block size for the vorticity field. Red indicates clockwise vorticity and blue counter clockwise vorticity. The system was initialized with a reduced mass density of $d = 1/7$. The system was at rest at $t = 0$, and was accelerated to the right by external forcing resulting in a terminal flow velocity of $v = 0.3c$ at $t = 20,000$, shown in this figure. The diameter of the cylindrical obstacle is 256ℓ lattice units. The critical Reynolds number for vortex shedding, $\mathrm{Re} = 42$, was achieve at approximately $t = 10,000$ time steps into the simulation. The maximum Reynolds number achieved in simulation is about $\mathrm{Re} \sim 250$.

4.2 Model Analysis

The FHP collision term is

$$\Omega_a^{\mathrm{FHP}} \equiv \Omega_a^{m=2,\vec{p}=0} + \Omega_a^{m=3,\vec{p}=0}. \tag{4.1}$$

The two-body term is

$$\Omega_a^{m=2,\vec{p}=0} = \alpha n_{a+1} n_{a+4} (1-n_a)(1-n_{a+2})(1-n_{a+3})(1-n_{a+5})$$

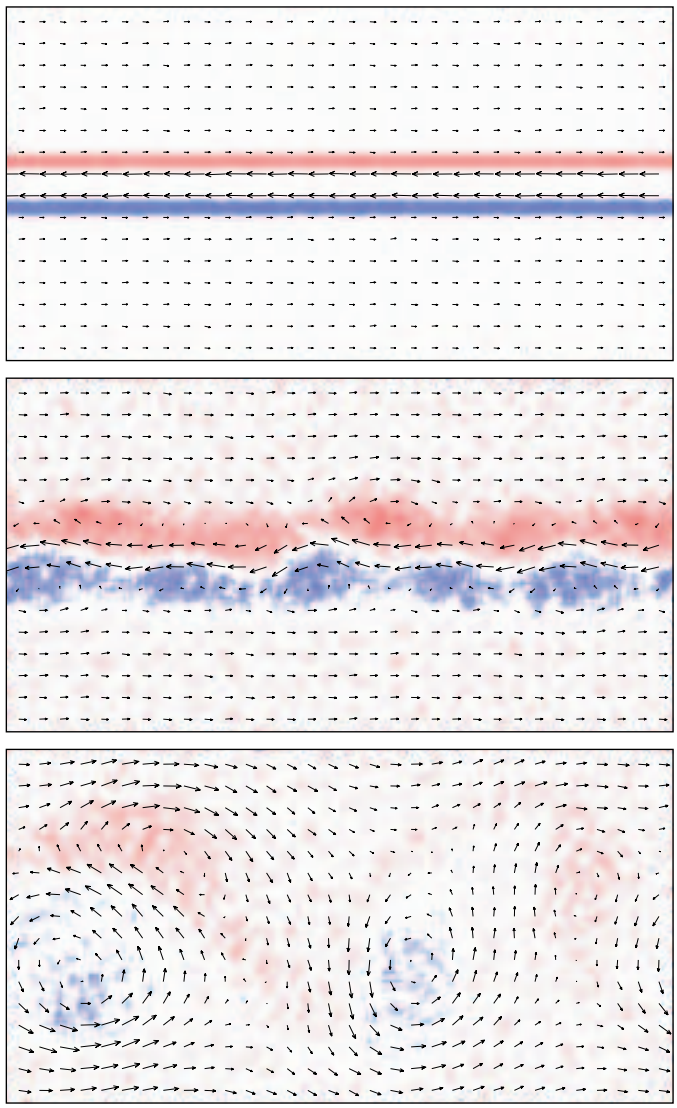

Figure 4.3: Classical lattice-gas fluid simulation with about 10 million particles computed on the CAM-8. Vorticity and momentum fields of the two-dimensional shear instability are shown. The simulation was done using a lattice size of 4096×2048 with toroidal boundary conditions, with spacetime averaging over 128x128 blocks for 50 time steps. FHP collisions with spectators and a rest particle were implemented. Macroscopic scale data is presented at 0, 10000, and 30000 time steps, which is at a Reynolds number of approximately Re ~ 1000.

$$
\begin{aligned}
&+ \quad (1-\alpha) n_{a+2} n_{a+5} (1-n_a)(1-n_{a+1})(1-n_{a+3})(1-n_{a+4}) \\
&- \quad n_a n_{a+3} (1-n_{a+1})(1-n_{a+2})(1-n_{a+4})(1-n_{a+5}),
\end{aligned} \tag{4.2}
$$

where $\alpha \in \{0,1\}$ is chosen uniformly randomly and and the symmetric 3-body term is

$$
\begin{aligned}
\Omega_a^{m=3,\vec{p}=0} &= n_{a+1} n_{a+3} n_{a+5} (1-n_a)(1-n_{a+2})(1-n_{a+4}) \\
&- n_a n_{a+2} n_{a+4} (1-n_{a+1})(1-n_{a+3})(1-n_{a+5}).
\end{aligned} \tag{4.3}
$$

The indices are taken modulo B. Writing $\Omega_a^{\text{FHP}}(n_*)$ with and asterisk subscript on n_* denotes that the collision term for the ath local state depends on all the on-site local states.

The Jacobian of the mesoscopic mean-field collision term for the FHP lattice gas is a circulant matrix[2]

$$
J^{\text{FHP}} = \begin{pmatrix}
-d(1-d)^2 & \frac{1}{2}d(1+d)(1-d)^2 & \frac{1}{2}d(1-3d)(1-d)^2 & -d(1-2d)(1-d)^2 & \frac{1}{2}d(1-3d)(1-d)^2 & \frac{1}{2}d(1+d)(1-d)^2 \\
\frac{1}{2}d(1+d)(1-d)^2 & -d(1-d)^2 & \frac{1}{2}d(1+d)(1-d)^2 & \frac{1}{2}d(1-3d)(1-d)^2 & -d(1-2d)(1-d)^2 & \frac{1}{2}d(1-3d)(1-d)^2 \\
\frac{1}{2}d(1-3d)(1-d)^2 & \frac{1}{2}d(1+d)(1-d)^2 & -d(1-d)^2 & \frac{1}{2}d(1+d)(1-d)^2 & \frac{1}{2}d(1-3d)(1-d)^2 & -d(1-2d)(1-d)^2 \\
-d(1-2d)(1-d)^2 & \frac{1}{2}d(1-3d)(1-d)^2 & \frac{1}{2}d(1+d)(1-d)^2 & -d(1-d)^2 & \frac{1}{2}d(1+d)(1-d)^2 & \frac{1}{2}d(1-3d)(1-d)^2 \\
\frac{1}{2}d(1-3d)(1-d)^2 & -d(1-2d)(1-d)^2 & \frac{1}{2}d(1-3d)(1-d)^2 & \frac{1}{2}d(1+d)(1-d)^2 & -d(1-d)^2 & \frac{1}{2}d(1+d)(1-d)^2 \\
\frac{1}{2}d(1+d)(1-d)^2 & \frac{1}{2}d(1-3d)(1-d)^2 & -d(1-2d)(1-d)^2 & \frac{1}{2}d(1-3d)(1-d)^2 & \frac{1}{2}d(1+d)(1-d)^2 & -d(1-d)^2
\end{pmatrix}. \tag{4.4}
$$

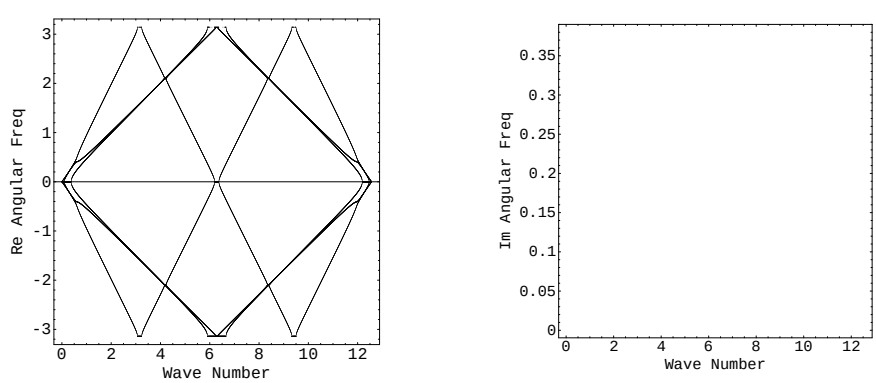

Figure 4.4: Dispersion relations for the FHP lattice gas for $\vec{k}$ along the $\hat{x}$-axis direction, $\omega = \omega(\rho, k_x)$ at a background density of $\rho = 2.5$. The real part of $\omega(k_x)$, plotted on the left, indicates propagating modes, and the imaginary part of $\omega(k_x)$, plotted on the right, indicates two damped soft excitations with parabolic dispersion relations at $k_x \sim 0$ and spurious modes at finite k_x. The periodicity of the reciprocal lattice is observed in this numerical solution, for example inversion symmetry $\omega(-\vec{k}) = \omega(\vec{k})$.

For the FHP lattice gas there are three soft modes, one corresponding to conservation mass and two corresponding to the two conserved components of momentum. The kinetic modes which are nonvanishing at first order cause damping in the lattice gas and are attributed to a positive imaginary part of ω, ($\text{Im}(\omega) > 0$). There are three hard modes corresponding the transport coefficients of the bulk, shear, and cubic viscosities, and in the long wavelength limit, the shear and cubic viscosities coincide for an isotropic fluid.

[2] It is sometimes possible to go beyond this Boltzmann approximation to determine a more accurate form of J by accounting for the particle-particle correlations, which arise from on-site collisions at the microscopic scale. This is called *renormalization*, and it which give rise to corrections the Boltzmann estimates of the transport coefficients. Renormalization theory for lattice gases has been worked out by Ernst *et al.* [29, 31] and by Boghosian [88] who has developed diagrammatic expansion methods for determining a renormalized J. Various approximations to sum terms involving higher and higher order particle-particle correlations, including the ring collisions for example, in certain cases are necessary to correctly estimate the value of the transport coefficients of a lattice-gas system. However, the renormalization of J is not necessary for single-speed lattice gases where the Boltzmann estimates are quite accurate.

Figures 4.5 shows a smaller region of the k-space within the first Brillouin zone of the reciprocal lattice where the long wavelength behavior of the system is apparent. A sound mode is observed in the real part of ω. For $\vec{k}$ along x and y-axis, the dispersion relation in the long wavelength limit predicts a sound speed of $c_s = \frac{c}{\sqrt{2}}$, which agrees with the numerical measurements. Since c_s is the same when the wave vector is aligned with either the x or y-axes, this indicates that the sound mode is isotropic, see the L.H.S. of Figures 4.5 and 4.6. The imaginary part of ω is parabolic at $\vec{k} \to 0$. This is characteristic of a viscous hydrodynamics regime with diffusive ordering, see the R.H.S. of Figures 4.5 and 4.6. In the viscous hydrodynamic regime, the dispersion relations for sound mode in the FHP lattice gas is found to be

$$\omega(\vec{k}) = \pm c_s k + i\Gamma(\rho)k^2. \tag{4.5}$$

Higher resolution plots of the dispersion curves, for a large range of background mass densities, are shown in Figure 4.13. We numerically fit the shallowest mode with a parabola. This gives us a way to determine the damping constant of compressional mass density waves. This result is given in §4.3.3

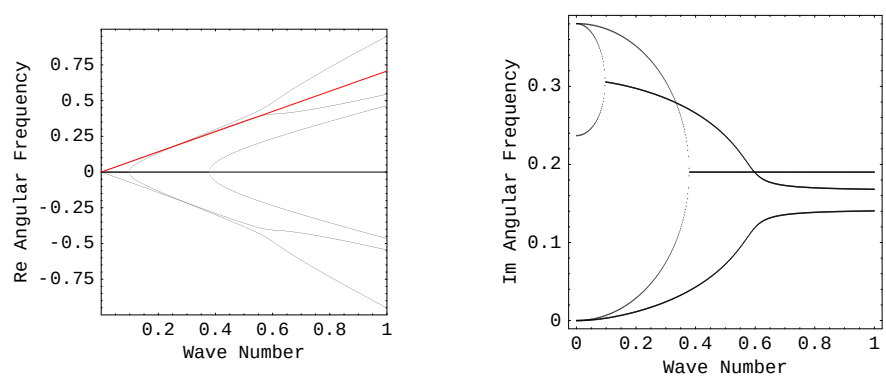

Figure 4.5: Dispersion relations for the FHP lattice gas for $\vec{k}$ along the $\hat{x}$-axis direction, $\omega = \omega(\rho, k_x)$ at a background density of $\rho = 2.5$ and for $k_x \leq 1$. In the long wavelength limit ($\vec{k} \to 0$), the real part of $\omega(k_x)$, plotted on the left, predicts a propagating excitation which is the sound mode with a linear dispersion relation $\Re\{\omega(k_x)\} = \pm c_s k_x$ with sound speed $c_s = \frac{1}{\sqrt{2}}$. The imaginary part of $\omega(k_x)$, plotted on the right, indicates two damped soft excitations with parabolic dispersion relations at $k_x \to 0$. The lowest parabola indicates sound damping with the dispersion relation, $\Im\{\omega(k_x)\} = \Gamma k_x^2$, which is plotted in more detail and for a range of densities in Figure 4.11.

Here we illustrate the identity (2.24)

$$J^{-1}|e_i e_j\rangle = \frac{1}{\kappa_\eta}|e_i e_j\rangle \tag{4.6}$$

using the well-known two-dimensional FHP lattice-gas model [2]. Using the x and y components of $\hat{e}_a = \left(\cos\frac{\pi a}{3}, \sin\frac{\pi a}{3}\right)$ separately, we define the following two kets

$$\begin{aligned} |e_x\rangle &\equiv \frac{1}{2}(1, -1, -2, -1, 1, 2) \\ |e_y\rangle &\equiv \frac{\sqrt{3}}{2}(1, 1, 0, -1, -1, 0). \end{aligned}$$

The direct product of $|e_i\rangle$ and $|e_j\rangle$ for $(i, j) \in (x, y)$ component by component gives

$$|e_x e_y\rangle = \frac{\sqrt{3}}{4}(1, -1, 0, -1, 1, 0) \tag{4.7}$$

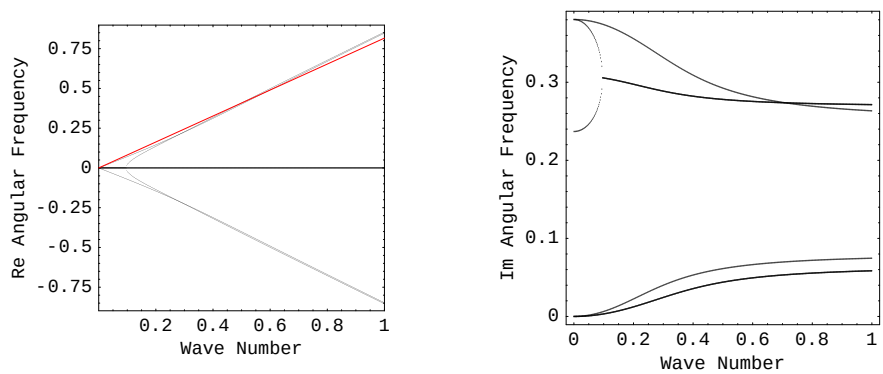

Figure 4.6: Dispersion relations for the FHP lattice gas for $\vec{k}$ along the $\hat{y}$-axis direction, $\omega = \omega(\rho, k_y)$ at a background density of $\rho = 2.5$. In the long wavelength limit ($\vec{k} \to 0$), the real part of $\omega(k_y)$, plotted on the left, predicts a propagating excitation which is the sound mode with a linear dispersion relation $\Re\{\omega(k_y)\} = \pm c_s k_y = c_s 2\pi \frac{2}{\sqrt{3}\lambda}$ with sound speed $c_s = \frac{1}{\sqrt{2}}$. The factor of $\sin(\frac{\pi}{3}) = \frac{\sqrt{3}}{2}$ comes about because the triangular lattice's cell size is shorter than it is wide by this amount. The imaginary part of $\omega(k_x)$, plotted on the right, indicates two damped soft excitations with parabolic dispersion relations at $k_x \to 0$. The lowest parabola indicates sound damping with the dispersion relation, $\Im\{\omega(k_y)\} = \Gamma k_y^2$. At $k_y \to 0$, this is identical to the dispersion relation with wave vector along the $\hat{x}$-axis indicating an isotropic sound mode.

$$|e_x e_x\rangle = \frac{\sqrt{1}}{4}(1,1,4,1,1,4) \tag{4.8}$$

$$|e_y e_y\rangle = \frac{\sqrt{3}}{4}(1,1,0,1,1,0). \tag{4.9}$$

Following Wolfram [1], we take the basic approach that the eigenkets of the linearized collision operator, which is the circulant matrix for the FHP model, have the form

$$|\alpha\rangle = \begin{pmatrix} e^{i\frac{\pi\alpha}{3}} \\ -e^{-i\frac{\pi\alpha}{3}} \\ (-1)^\alpha \\ -e^{i\frac{\pi\alpha}{3}} \\ e^{-i\frac{\pi\alpha}{3}} \\ 1 \end{pmatrix}, \tag{4.10}$$

for $\alpha = 1, 2, \ldots, 6$. We are free to define a new set of eigenkets by taking linear combinations of $|\alpha\rangle$ so that we can express the eigenkets of J^{FHP} in terms of the lattice kets $|e_x\rangle$, $|e_y\rangle$, $|e_x e_x\rangle$, $|e_y e_y\rangle$, and $|e_x e_y\rangle$. This is done as follows

$$\begin{aligned}
|1'\rangle &= |6\rangle = (1,1,1,1,1,1) = |e_x e_x\rangle + |e_y e_y\rangle \\
|2'\rangle &= \frac{1}{i\sqrt{3}}(|1\rangle - |5\rangle) = (1,1,0,-1,-1,0) = \frac{2}{\sqrt{3}}|e_y\rangle \\
|3'\rangle &= |1\rangle + |5\rangle = (1,-1,-2,-1,1,2) = 2|e_x\rangle \\
|4'\rangle &= |2\rangle - |4\rangle = (1,1,-2,1,1,-2) = 2(|e_y e_y\rangle - |e_x e_x\rangle) \\
|5'\rangle &= \frac{1}{i\sqrt{3}}(|2\rangle + |4\rangle) = (1,-1,0,1,-1,0) = \frac{4}{\sqrt{3}}|e_x e_y\rangle \\
|6'\rangle &= |3\rangle = (-1,1,-1,1,-1,1).
\end{aligned}$$

All the $\langle\alpha'|$ must be defined with the appropriate magnitude to satisfy the normality condition, $\langle\alpha'|\alpha'\rangle = 1$ for all α'. The mean-field collision operator for the FHP lattice gas is simply obtained

by replacing the n_a's in Equation (4.1) with f_a's. Using this in the eigenvalue formula (2.18)

$$\kappa_\alpha = \sum_{m=1}^{B} J_m e^{2\pi i m\alpha/B}, \tag{4.11}$$

it follows that the eigenvalues of J^{FHP} are

$$\begin{aligned}
\langle 1'|J^{\text{FHP}}|1'\rangle &= 0 \\
\langle 2'|J^{\text{FHP}}|2'\rangle &= 0 \\
\langle 3'|J^{\text{FHP}}|3'\rangle &= 0 \\
\langle 4'|J^{\text{FHP}}|4'\rangle &= -3d(1-d)^3 \\
\langle 5'|J^{\text{FHP}}|5'\rangle &= -3d(1-d)^3 \\
\langle 6'|J^{\text{FHP}}|6'\rangle &= 6d^2(1-d)^2.
\end{aligned}$$

Note that $\langle 1'|J^{\text{FHP}}|1'\rangle$ corresponds to mass conservation, $\langle 2'|J^{\text{FHP}}|2'\rangle$ to y-momentum conservation, and $\langle 3'|J^{\text{FHP}}|3'\rangle$ to x-momentum conservation. The degenerate viscous eigenvalue $\kappa_\eta = -3d(1-d)^3$ is immediately identified.

Using the eigenket of the kinetic subspace, we can compute the generalized inverse $(J^{\text{FHP}})^{-1}$ as follows

$$(J^{\text{FHP}})^{-1} = \underbrace{\begin{pmatrix} |4'\rangle & |5'\rangle & |6'\rangle \end{pmatrix}}_{(6\times 3 \text{ matrix})} \begin{pmatrix} \frac{1}{\kappa_{4'}} & 0 & 0 \\ 0 & \frac{1}{\kappa_{5'}} & 0 \\ 0 & 0 & \frac{1}{\kappa_{6'}} \end{pmatrix} \underbrace{\begin{pmatrix} \langle 4'| \\ \langle 5'| \\ \langle 6'| \end{pmatrix}}_{(3\times 6 \text{ matrix})}. \tag{4.12}$$

We have

$$(J^{\text{FHP}})^{-1} = \begin{pmatrix}
\frac{1+3\,d}{36\,(-1+d)^3\,d^2} & \frac{-(1+d)}{36\,(-1+d)^3\,d^2} & \frac{1-3\,d}{36\,(-1+d)^3\,d^2} & \frac{-1+5\,d}{36\,(-1+d)^3\,d^2} & \frac{1-3\,d}{36\,(-1+d)^3\,d^2} & \frac{-(1+d)}{36\,(-1+d)^3\,d^2} \\
\frac{-(1+d)}{36\,(-1+d)^3\,d^2} & \frac{1+3\,d}{36\,(-1+d)^3\,d^2} & \frac{-(1+d)}{36\,(-1+d)^3\,d^2} & \frac{1-3\,d}{36\,(-1+d)^3\,d^2} & \frac{-1+5\,d}{36\,(-1+d)^3\,d^2} & \frac{1-3\,d}{36\,(-1+d)^3\,d^2} \\
\frac{1-3\,d}{36\,(-1+d)^3\,d^2} & \frac{-(1+d)}{36\,(-1+d)^3\,d^2} & \frac{1+3\,d}{36\,(-1+d)^3\,d^2} & \frac{-(1+d)}{36\,(-1+d)^3\,d^2} & \frac{1-3\,d}{36\,(-1+d)^3\,d^2} & \frac{-1+5\,d}{36\,(-1+d)^3\,d^2} \\
\frac{-1+5\,d}{36\,(-1+d)^3\,d^2} & \frac{1-3\,d}{36\,(-1+d)^3\,d^2} & \frac{-(1+d)}{36\,(-1+d)^3\,d^2} & \frac{1+3\,d}{36\,(-1+d)^3\,d^2} & \frac{-(1+d)}{36\,(-1+d)^3\,d^2} & \frac{1-3\,d}{36\,(-1+d)^3\,d^2} \\
\frac{1-3\,d}{36\,(-1+d)^3\,d^2} & \frac{-1+5\,d}{36\,(-1+d)^3\,d^2} & \frac{1-3\,d}{36\,(-1+d)^3\,d^2} & \frac{-(1+d)}{36\,(-1+d)^3\,d^2} & \frac{1+3\,d}{36\,(-1+d)^3\,d^2} & \frac{-(1+d)}{36\,(-1+d)^3\,d^2} \\
\frac{-(1+d)}{36\,(-1+d)^3\,d^2} & \frac{1-3\,d}{36\,(-1+d)^3\,d^2} & \frac{-1+5\,d}{36\,(-1+d)^3\,d^2} & \frac{1-3\,d}{36\,(-1+d)^3\,d^2} & \frac{-(1+d)}{36\,(-1+d)^3\,d^2} & \frac{1+3\,d}{36\,(-1+d)^3\,d^2}
\end{pmatrix}. \tag{4.13}$$

Note that $(J^{\text{FHP}})^{-1}J^{\text{FHP}} \neq \mathbf{1}$, since $(J^{\text{FHP}})^{-1}$ is the generalized inverse of J^{FHP}

$$(J^{\text{FHP}})^{-1}J^{\text{FHP}} = \begin{pmatrix}
\frac{1}{2} & -\frac{1}{3} & 0 & \frac{1}{6} & 0 & -\frac{1}{3} \\
-\frac{1}{3} & \frac{1}{2} & -\frac{1}{3} & 0 & \frac{1}{6} & 0 \\
0 & -\frac{1}{3} & \frac{1}{2} & -\frac{1}{3} & 0 & \frac{1}{6} \\
\frac{1}{6} & 0 & -\frac{1}{3} & \frac{1}{2} & -\frac{1}{3} & 0 \\
0 & \frac{1}{6} & 0 & -\frac{1}{3} & \frac{1}{2} & -\frac{1}{3} \\
-\frac{1}{3} & 0 & \frac{1}{6} & 0 & -\frac{1}{3} & \frac{1}{2}
\end{pmatrix}. \tag{4.14}$$

However, if we compute the matrix of elements, we see that J^{-1} is indeed the inverse of J in the kinetic space

$$\langle \alpha'|(J^{\text{FHP}})^{-1}J^{\text{FHP}}|\alpha'\rangle = \begin{pmatrix}
0 & 0 & 0 & 0 & 0 & 0 \\
0 & 0 & 0 & 0 & 0 & 0 \\
0 & 0 & 0 & 0 & 0 & 0 \\
0 & 0 & 0 & 1 & 0 & 0 \\
0 & 0 & 0 & 0 & 1 & 0 \\
0 & 0 & 0 & 0 & 0 & 1
\end{pmatrix}. \tag{4.15}$$

Finally, we see that $|e_x e_y\rangle$ is an eigenvector of $(J^{\text{FHP}})^{-1}$, with eigenvalue $\frac{1}{\kappa_\eta} = \frac{-1}{3d(1-d)^3}$

$$(J^{\text{FHP}})^{-1}|e_x e_y\rangle = \frac{-1}{3d(1-d)^3}|e_x e_y\rangle. \tag{4.16}$$

The Hénon's shear viscosity formula (2.50) for a classical lattice gas is

$$\eta = \frac{\rho \ell_s^2}{\tau}\frac{1}{D+2}\left(\frac{1}{\kappa_\eta} - \frac{1}{2}\right). \tag{4.17}$$

Since $\kappa_\eta = -3d(1-d)^3$ for the FHP lattice gas, Equation (2.50) is

$$\eta^{\text{FHP}} = \rho\frac{\ell^2}{\tau}\left(\frac{1}{12d(1-d)^3} - \frac{1}{8}\right). \tag{4.18}$$

4.3 Comparing Analytical and Numerical Predictions

4.3.1 Single-Particle Probability of Occupancy in the Subsonic Limit

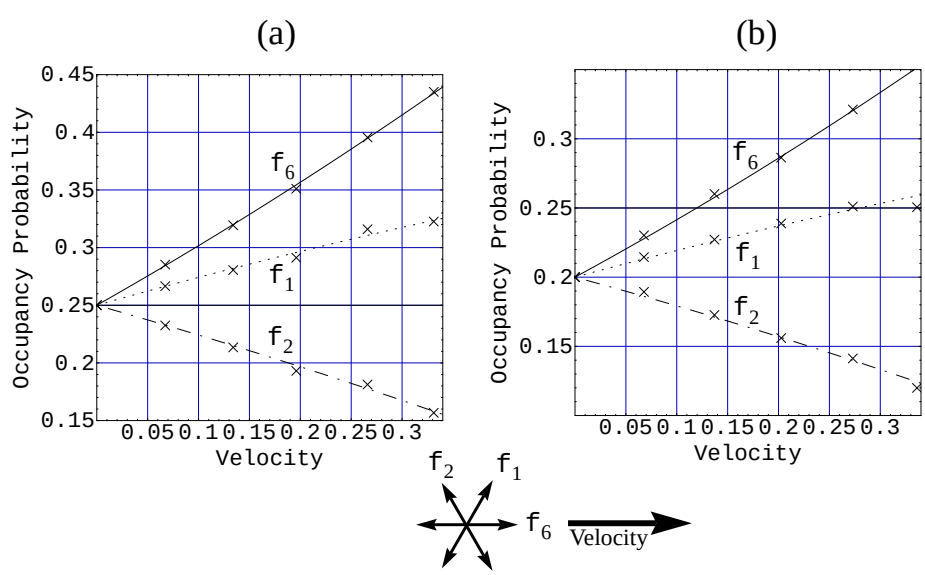

Figure 4.7: Theory versus simulation comparison of the velocity dependence of the single-particle distribution function in the non-Galilean parameterization: $f_a = d + dD\hat{e}_a \cdot \vec{v} + gdD(D/2+1)\hat{Q}_a : \vec{v}\vec{v}$. FHP simulation data is overplotted on this predicted mesoscopic probability of occupancy. Plots (a) and (b) are for reduced background densities of $d = .20$ and $d = 0.25$, respectively. A velocity shift is imparted along the x-axis; that is, along the f_1 direction indicated in the figure. Data was collected from a 128×128 classical FHP simulation (crosses) and was coarse-grained averaged over 1600 time steps from time step $t = 400$ to $t = 2000$.

The general form of the single-particle occupancy probability, appropriate for single speed lattice gases, is a Fermi-Dirac function whose argument is the sum of scalar collision invariants, $\alpha\rho + \beta\hat{e}_a \cdot \vec{p} + \gamma E$ [3]

$$f_a^{\text{eq}} = \frac{1}{1 + e^{\alpha\rho + \beta\hat{e}_a\cdot\vec{p} + \gamma E}}. \tag{4.19}$$

Fundamentally, this arises because the individual classical bits representing particles satisfy a Pauli exclusion principle. By Taylor expanding (4.19) about $\vec{v} = 0$ to fourth order in the velocity and

equating the zeroth, first, and second moments of f_a respectively, the parameters α and β are determined [3]. The result of the low Mach number expansion of $f_a^{\rm eq}$ is

$$(f_a^{\rm eq})^{ideal} = \frac{n}{B} + \frac{nD}{cB} e_{ai} v_i + g \frac{nD(D+2)}{2c^2 B} e_{ai} e_{aj} v_i v_j - g \frac{n(D+2)}{2c^2 B} v^2 + \mathcal{O}(M^3), \tag{4.20}$$

where the density dependent Galilean prefactor is

$$g(d) = \frac{D}{D+2} \frac{1-2d}{1-d}. \tag{4.21}$$

The predicted functional form (4.20) is checked in the subsonic limit against numerical data taken from a simulation of a classical FHP lattice gas. The analytical and numerical results are in excellent agreement and are shown in Figure 4.7.

Using $\rho = mn$ for the density and $c_s = \frac{c}{\sqrt{D}}$ for the sound speed, the moments of lattice gas distribution are

$$m \sum_a (f_a^{eq})^{ideal} = \rho \tag{4.22}$$

$$mc \sum_a e_{ai} (f_a^{eq})^{ideal} = \rho v_i \tag{4.23}$$

$$mc^2 \sum_a e_{ai} e_{aj} (f_a^{eq})^{ideal} = \rho c_s^2 (1 - g \frac{v^2}{c^2}) \delta_{ij} + g \rho v_i v_j. \tag{4.24}$$

Note that for a uniform filling of states, $f_a = d$ for all directions and so $\vec{v} = 0$, then[3]

$$\rho(\vec{x}, t) = mBd \tag{4.25}$$

$$v_i(\vec{x}, t) = 0 \tag{4.26}$$

$$\Pi_{ij}(\vec{x}, t) = \rho c_s^2 \delta_{ij}. \tag{4.27}$$

This is expected since when $v_i = 0$, the momentum flux density tensor is diagonal and scales with the pressure ($\Pi_{ij} = P\delta_{ij}$) and for an ideal gas $P = \rho c_s^2$.

4.3.2 Measuring the Shear Viscosity Using the Decay of a Sinusoidal Shear Wave

Given a sinusoidal perturbation of wavelength λ of a fluid one can straightforwardly measure the time for relaxation to an equilibrium state where the fluid is at rest. This method was used to measure the shear viscosity of the FCHC lattice gas by Adler *et al.* [22]. The relevant part of the Navier-Stokes equation is the time dependent term and the momentum diffusion term

$$(\partial_t - \nu \partial_y^2) p_x = 0. \tag{4.28}$$

This has the solution

$$p_x = p_o \sin(ky) e^{-k^2 \nu t}. \tag{4.29}$$

Therefore, the decay rate, $k^2\nu$, can be measured to determine ν since $k = \frac{2\pi}{\lambda}$ is known. This method is easier to implement on the CAM-8 than the square-wave forcing method used by Kadanoff, McNamara, and Zanetti [20], since no forcing bits or rules are required and it is easy to generate an initial random fluid pattern with a sinusoidal perturbation. Very good agreement is found between the mean-field prediction of the kinematic shear viscosity and the numerical data shown in Figure 4.10 taken on the CAM-8 for the FHP lattice gas.

[3] We used the following property of the displacement vectors, $\sum_a \hat{e}_a = 0$ and $\sum_a e_{ai} e_{aj} = \frac{B}{D} \delta_{ij}$, that was originally derived by Wolfram [1]

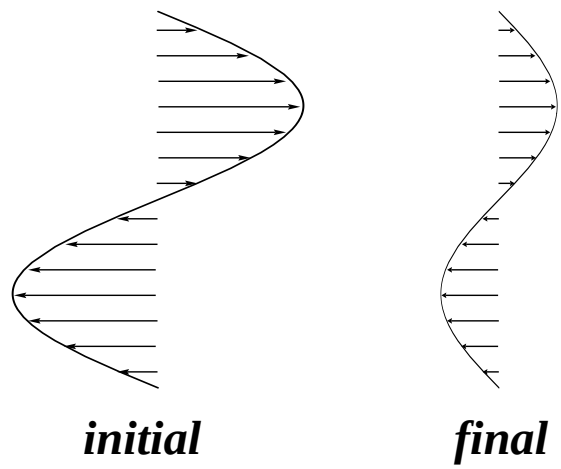

Figure 4.8: A depiction of an intial sinusoidal shear wave perturbation that decays over time to a final state with a smaller amplitude.

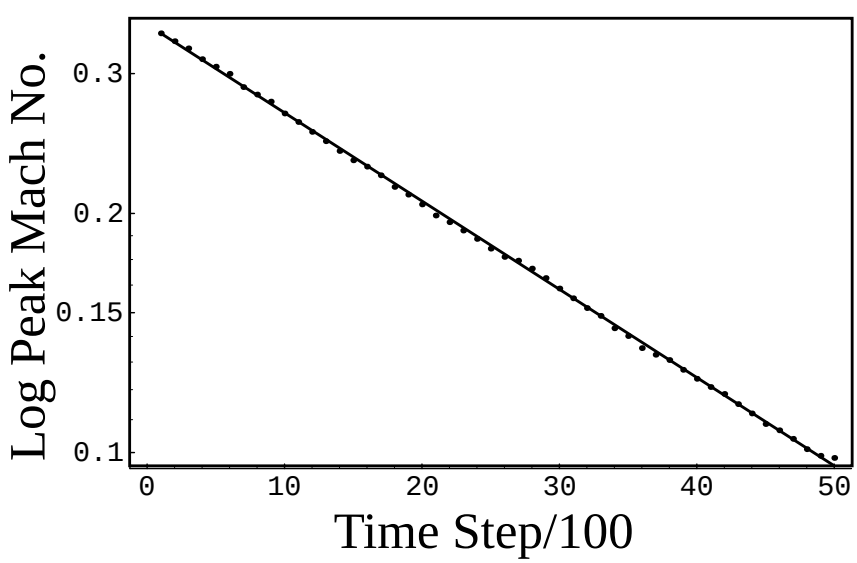

Figure 4.9: Plot of the amplitude of a shear wave versus time. The amplitude of shear wave of the momentum density field decays exponentially as is shown here on a log-linear plot. Linear regression is used to fit the data set and the predicted the decay exponent, which is proportional to the kinematic shear viscosity of the lattice-gas fluid. Data is taken from a 512×512 classical FHP simulation at a background density of $d_\circ = 0.15$.

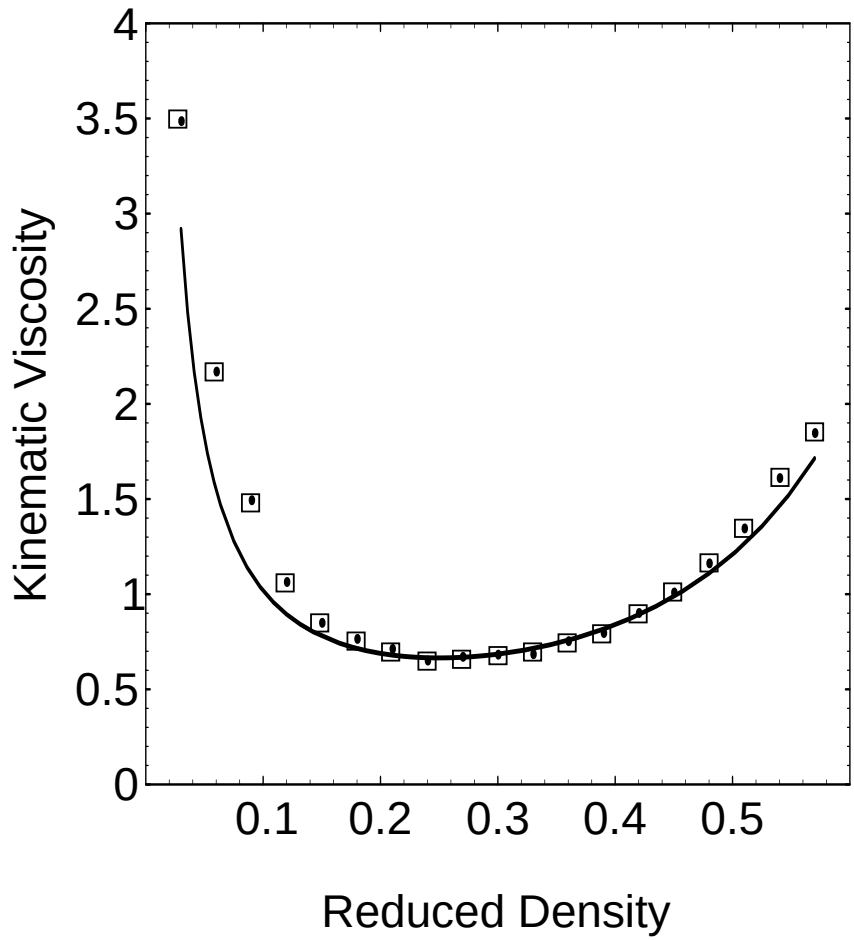

Figure 4.10: Kinematic viscosity versus density obtained by measuring the rate of exponential damping of a sinusoidal velocity perturbation. The theoretical mean-field prediction and numerical data are plotted for an FHP lattice gas with 2 and 3-body collisions on a two dimensional triangular lattice. Simulation runs were done on the CAM-8 on a 512×512 periodic space.

4.3.3 Measuring the Bulk Viscosity Using the Decay of a Sinusoidal Compressional Wave

In the viscous hydrodynamic regime, the dispersion relations for sound mode in the FHP lattice gas has the form

$$\omega(\vec{k}) = \pm c_s k + i\Gamma(\rho)k^2.$$

We can determine the damping constant by solving for the roots of the secular determinant of the linearized Boltzmann equation in k-space. Our predicted value of the damping constant are gotten by a numerical fitting procedure shown in Figure 4.11. In this case, the analysis was carried out with the wave vector of the density perturbation aligned with the x-axis of the Bravais lattice. The procedure was repeated for a density perturbation along the y-axis, and the same result was obtained. This indicates that the sound mode of the FHP lattice gas is isotropic in the long wavelength limit where diffusive ordering holds.

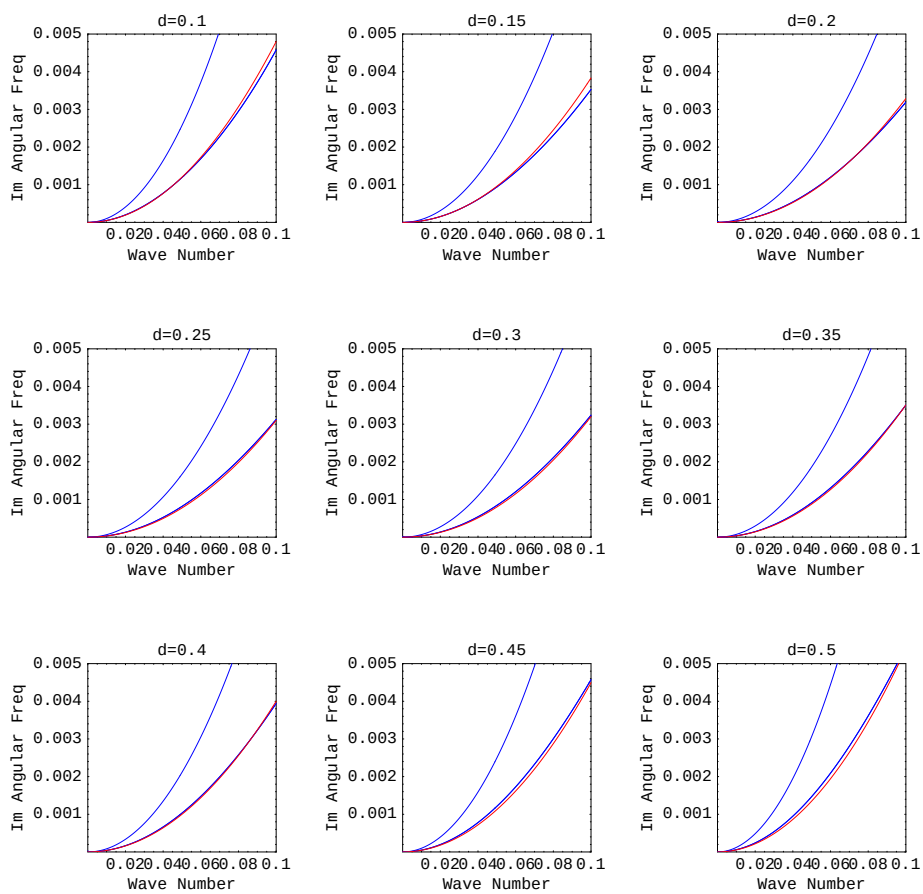

Figure 4.11: Imaginary part of the dispersion relation, $\omega = \omega(\rho, k_x)\}$, for the FHP lattice gas. The wave vector is directed along the $\hat{x}$-axis, $\vec{k} = k_x\hat{x}$, and the results are plotted for a range of background densities from $\rho_\circ = 0.6$ to $\rho = 3$. The lowest curves are numerically fit with a parabola, which are plotted in red. Since the dispersion relation is $\Im\{\omega(k_y)\} = \Gamma k_x^2$ in the long wavelength limit, we can predict the damping constant as a function of mass density, $\Gamma = \Gamma(\rho)$. This analytical prediction of $\Gamma(\rho)$ agrees well with data from numerical measurements taken from the lattice-gas simulation. See Figure 4.13.

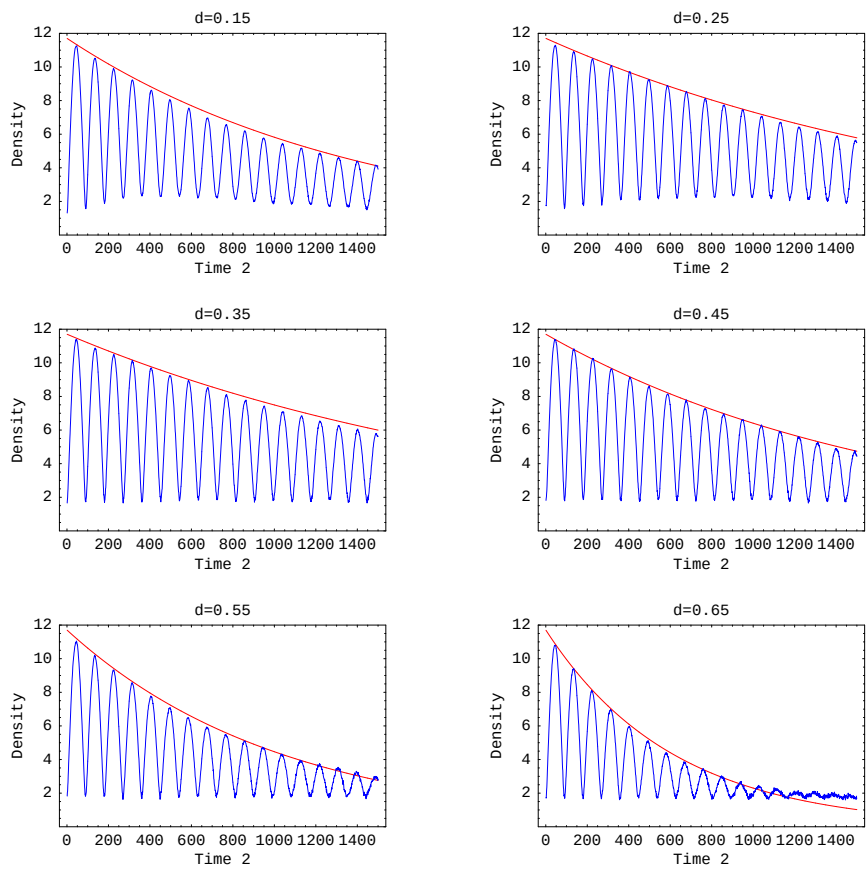

Figure 4.12: Sound wave density oscillations, depicted in blue, measured from classical FHP lattice-gas simulations carried out for a range of reduced background densities, $d = 0.15$ to $d = 0.65$. Initially, the density field has a sinusoidal perturbation of size $\lambda = 256$ with an amplitude of $\delta d = 0.1$ and with its wave vector directed along the $\hat{x}$-axis, $\vec{k} = (k, 0)$. The simulation was carried out on a 256×256 triangular lattice for $t = 3000$ time steps, and data was sampled at every other time step. The amplitude of the sound wave decays exponentially fast, $\delta\rho = \delta\rho_\circ e^{ikc_s t - k^2 \Gamma t}$, where the wave number is $k = \frac{2\pi}{\lambda}$ and the sound speed is $c_s = \frac{\ell}{\tau\sqrt{2}}$. The damping constant, Γ, is determined by a numerical fit to the envelope of the oscillation, and the resulting exponential curve is overplotted in red.

The time evolution of a sinusoidal mass density perturbation of wavelength $\lambda = 256$ in a 256 size system (with periodic boundary conditions imposed) was simulated with a microscopic FHP lattice gas. To measure the damping constant, the simulation was run for 3000 time steps and the amplitude of the resulting compressional standing wave was record. The time series data is plotted in Figure 4.12 for a range of background densities. The envelope of the oscillation is a decaying exponential curve. This decay constant is $-k^2\Gamma(\rho)$. In this way, numerical fitting allows us to determine the sound damping constant, $\Gamma(\rho)$, as a function of mass density. The numerical results measured from an FHP lattice-gas simulation are compared with Boltzmann predictions for a range of reduced density from $d = 0.15$ to 0.75. The comparison is shown in Figure 4.13. The agreement between simulation and theory is good.

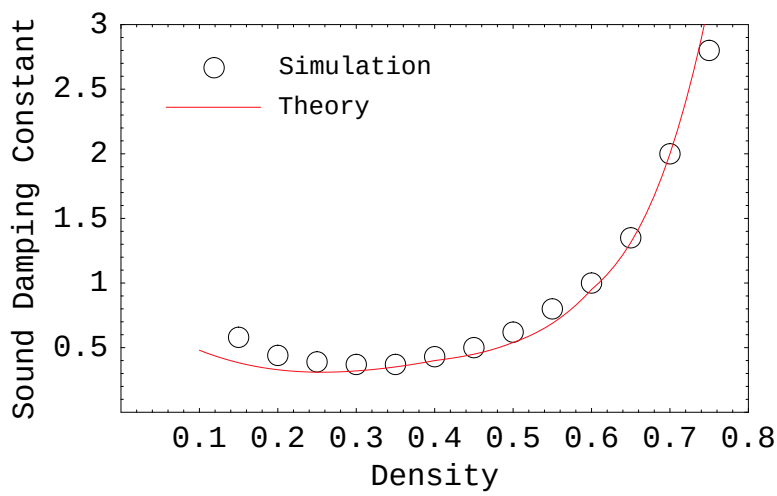

Figure 4.13: Comparison of theory versus simulation for the classical FHP lattice gas. The analytical curve (plotted in red) is calculated from a detailed analysis of the linearized Boltzmann equation. The sound damping constant is predicted in the long wavelength limit as is shown in Figure 4.11. The numerical data (plotted as circles) is calculated from an FHP lattice-gas simulation using the method of relaxation of a mass density field standing wave as is shown in Figure 4.12. The two methods of determining the coefficient of sound damping are in good agreement.

The constancy of the sound speed was also using the data taken from the compressional wave test. It appears that c_s for the microscopic FHP lattice gas is independent of density. See Figure 4.14.

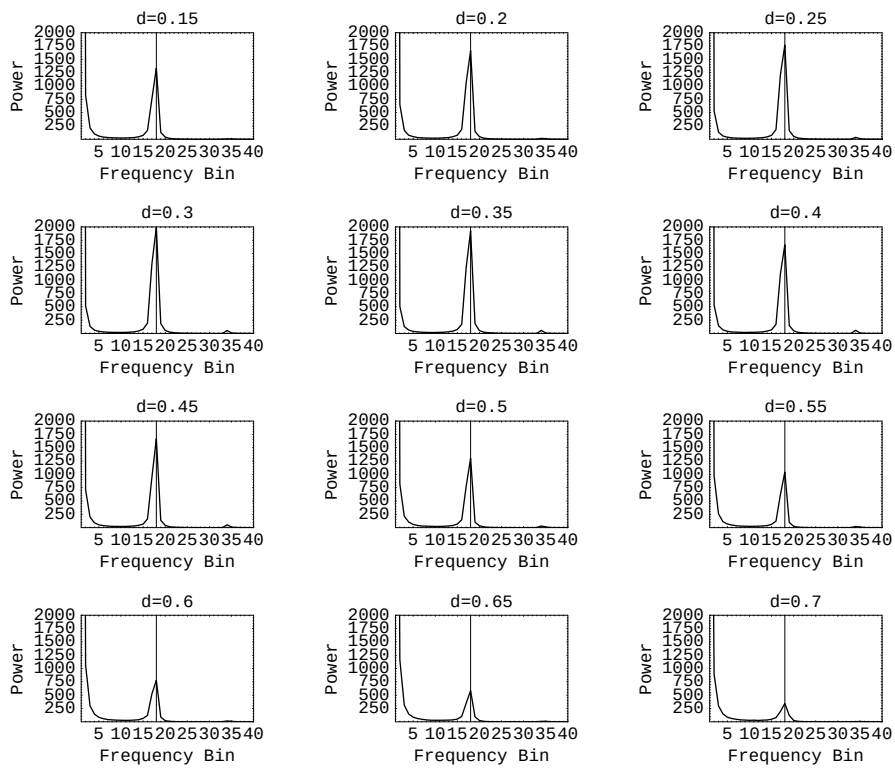

Figure 4.14: Plot of the power spectrum, $\rho_k^* \rho_k$, computed using the discrete Fourier transform of a mass density field standing wave for a range of reduced background densities from $d = 0.15$ to $d = 0.7$. Measurements were taken from classical FHP lattice-gas simulations on a 256×256 grid. The size of the standing wave is $\lambda = 256$ and it oscillates and decays over time (see Figure 4.12). The peak in the power spectrum occurs at the same location corresponding to a density-independent sound speed.

Chapter 5

Conclusion

We have presented a review of the classical lattice-gas method that included a description of how one may analytically predict certain fluid-like behaviors in the long wavelength limit. We have also included a description of two lattice-gas models using one and two-dimensional lattices as examples. A linearized lattice-Boltzmann equation at the mesoscopic scale is used to calculate the dispersion relations for the sound mode and shear and bulk viscosity modes of the dynamical lattice-gas system. For small wave numbers, these dispersion relations are compared to numerical data taken from both large-scale and slow modes present in the two lattice-gas models. Numerical and analytical predictions of the sound damping constant and sound speed are in agreement and diffusive ordering of damping times versus grid size is observed in this context. Furthermore, numerical and analytical predictions for the shear and bulk viscosities for the two-dimensional lattice-gas system were compared and are in good agreement as well.

The numerical efficiency and convergence properties of the lattice-gas algorithm are not reported in the chapters covering the numerical simulations. Therefore, it is important to state here that the computational efficiency and the order of convergence of the lattice-gas algorithm implemented on classical general-purpose computers is much lower than that achievable by computational fluid dynamics codes implemented on the same general-purpose computers using high-level languages based on floating-point representations of real valued quantities. A significant speed-up of the lattice-gas algorithm can be achieved using simple special-purpose computers [104, 105]. However, the gains are not sufficient to warrant the continued construction of these special-purpose classical computers, except perhaps for use in the narrowly defined application area of the computational fluid dynamics of multispecies and multiphase lattice-gas systems and for use in understanding the extent to which reversible algorithms (a special case of unitary algorithms) applied over massively large data sets can be used for physical modeling purposes.

Appendix A

Small Mach Number Expansion of the Occupancy Probability

The single-particle distribution function has the form

$$f(z_a) = \frac{1}{z_a + 1}, \tag{A.1}$$

where the natural log of the *fugacity*

$$\ln z_a = \alpha\rho + \beta\hat{e}_a \cdot \vec{p} + \gamma E \tag{A.2}$$

is a linear combination of the conserved scalar quantities, the mass ρ,the momentum component $\hat{e}_a \cdot \vec{p}$ along the lattice direction $\hat{e}_a$, and the energy E at a lattice site. The real numbered coefficients α, β, and γ are free parameters that we will determine. It is convenient to define the momentum and energy independent part of the fugacity as

$$z_\circ \equiv e^{\alpha\rho}. \tag{A.3}$$

Since $f_a(z_\circ) = d$ is the reduced density, $d \equiv \frac{\rho}{mB}$, we must set

$$z_\circ = \frac{1-d}{d}. \tag{A.4}$$

This fixes the coefficient α. To fix the coefficients β and γ, we can specify two moments of the single-particle distribution function as constraint conditions. We begin by Taylor expanding the single-particle distribution function $f(z_a)$ about $z_\circ$

$$f(z_a) = d + f'(z_\circ)\delta z + \frac{1}{2}f''(z_\circ)(\delta z^2) + \cdots. \tag{A.5}$$

The derivative of f evaluated at $z_\circ$ are

$$f'(z) = \frac{-1}{(z+1)^2} \longrightarrow f'(z_\circ) = -d^2 \tag{A.6}$$

and

$$f''(z) = \frac{2}{(z+1)^3} \longrightarrow f''(z_\circ) = 2d^3, \tag{A.7}$$

so

$$f(z_a) \cong d\left[1 - d\delta z + d^2(\delta z)^2\right]. \tag{A.8}$$

To determine δz, we begin by writing the fugacity in series form

$$z_a = z_\circ \left[\sum_{k=0}^{\infty} \frac{(\beta \hat{e}_a \cdot \vec{p})^k}{k!}\right] \left[\sum_{k=0}^{\infty} \frac{(\gamma E)^k}{k!}\right]. \tag{A.9}$$

In the subsonic limit, $\vec{p} \ll mc$, keeping terms only to second order in the velocity, the fugacity becomes

$$z_a = z_\circ \left[1 + \beta \hat{e}_a \cdot \vec{p} + \frac{1}{2}(\beta \hat{e}_a \cdot \vec{p})^2\right](1 + \gamma E) + \mathcal{O}(v^3). \tag{A.10}$$

since $p \sim v$ and $E \sim v^2$. Then to second order in the velocity, the change in z_a is

$$\delta z_a \equiv z_a - z_\circ = \left(\frac{1-d}{d}\right)\left[\beta \hat{e}_a \cdot \vec{p} + \frac{1}{2}(\beta \hat{e}_a \cdot \vec{p})^2 + \gamma E\right] + \mathcal{O}(v^3) \tag{A.11}$$

and the square of the change is

$$(\delta z_a)^2 = \left(\frac{1-d}{d}\right)^2 \beta^2 \left(\hat{e}_a \cdot \vec{p}\right)^2 + \mathcal{O}(v^3). \tag{A.12}$$

Inserting the expressions for δz and $(\delta z)^2$ into the Taylor expansion of $f(z_a)$ we have

$$\begin{aligned} f(z_a) &= d\left\{1 - (1-d)\left[\beta \hat{e}_a \cdot \vec{p} + \frac{1}{2}(\beta \hat{e}_a \cdot \vec{p})^2 + \gamma E\right] + (1-d)^2 \left(\hat{e}_a \cdot \vec{p}\right)^2\right\} \\ &= d\left[1 - (1-d)\left(\beta \hat{e}_a \cdot \vec{p} + \gamma E\right) + \frac{1}{2}(1-d)(1-2d)\beta^2 \left(\hat{e}_a \cdot \vec{p}\right)^2\right]. \end{aligned} \tag{A.13}$$

We have the freedom to choose the coefficients β and γ to parameterized the distribution function as we see fit to satisfy any two constraints. Consider a parameterization that fixes the value of the coefficients β and γ by using the following moments for the mass density and momentum density

$$\rho = m \sum_{a=1}^{B} f_a \tag{A.14}$$

$$\rho \vec{v} = mc \sum_{a=1}^{B} \hat{e}_a f_a. \tag{A.15}$$

The parameterization may be termed the *non-Galilean parametrization*. Constraints Equations (A.14) and (A.15) are typically used in the formulation of classical lattice gases. The single particle distribution function using this non-Galilean parameterization was first found in the mid 1980's by the US researchers Wolfram and Hasslacher and by the French researchers Frisch, d'Humières, Lallemand, Pomeau, and Rivet [1, 3]. Their derivation of Equation (A.20) is different then the derivation presented in this section; they used only two free coefficients in the expression for the fugacity, one for the mass and the other for the momentum; whereas we use three free coefficients. The reason for using only two free parameters is that in the standard single-speed classical lattice-gas construction, the energy is degenerate with the mass, so it was deemed unnecessary to keep a separate free coefficient for the energy. However, it is expedient to use a free parameter for E. Using Equations (A.14) and (A.15) as constraint equations gives us a non-unity density-dependent prefactor in the convective term in the hydrodynamic flow equation.

Inserting Equation (A.13) into Equation (A.15), the odd term in the distribution function expansion survives the first moment sum over lattice directions; the odd term is the one linear in the momentum. This fixes the value of β to be

$$\beta = -\frac{D}{1-d} \tag{A.16}$$

so the distribution function becomes

$$f_a = d\left[1 + D\hat{e}_a \cdot \vec{p} + \frac{D^2}{2}\frac{1-2d}{1-d}\left(\hat{e}_a \cdot \vec{p}\right)^2 + (1-d)\gamma E\right]. \tag{A.17}$$

Inserting Equation (A.17) into Equation (A.14), all the even terms that survive the sum over lattice directions must add to zero. This fixes the value of γ as follows

$$\frac{D}{2}\frac{1-2d}{1-d}p^2 - (1-d)\gamma E = 0 \tag{A.18}$$

or

$$\gamma E = D\frac{1-2d}{(1-d)^2}\frac{p^2}{2}. \tag{A.19}$$

Therefore, the non-Galilean parameterized distribution function is

$$f_a = d\left[1 + De_{ai}p_i + \frac{D(D+2)}{2}g(d)Q_{aij}p_ip_j\right], \tag{A.20}$$

where the density dependent prefactor $g(d)$ is defined

$$g(d) \equiv \frac{D}{D+2}\frac{1-2d}{1-d} \tag{A.21}$$

and the traceless second-rank tensor $\hat{Q}_a$ is defined

$$Q_{aij} \equiv e_{ai}e_{aj} - \frac{\delta_{ij}}{D}. \tag{A.22}$$

$\hat{Q}_a$ is an isotropic symmetric tensor. This mass-energy degeneracy leads to an anomalous description of the lattice-gas fluid's behavior. Let us see why. The second moment of Equation (A.20) gives the momentum flux density

$$mc^2\sum_{a=1}^{B} e_{ai}e_{aj}f_a = P\delta_{ij} + g\rho v_iv_j. \tag{A.23}$$

The density-dependent prefactor g appears in the nonlinear convective term, so this parametrization does indeed give rise to non-Galilean fluid flow. The pressure in Equation (A.23) has a spurious quadratic velocity dependence

$$P = \rho c_s^2\left(1 - g\frac{v^2}{c^2}\right). \tag{A.24}$$

Bibliography

[1] Stephen Wolfram. Cellular automaton fluids 1: Basic theory. *Journal of Statistical Physics*, 45(3/4):471–526, 1986.

[2] Uriel Frisch, Brosl Hasslacher, and Yves Pomeau. Lattice-gas automata for the navier-stokes equation. *Physical Review Letters*, 56(14):1505–1508, 1986.

[3] Uriel Frisch, Dominique d'Humiéres, Brosl Hasslacher, Pierre Lallemand, Yves Pomeau, and Jean-Pierre Rivet. Lattice gas hydrodynamics in two and three dimensions. *Complex Systems*, 1:649–707, 1987.

[4] Jean-Pierre Rivet, Michel Heńon, and Uriel Frisch. Simulating fully three-dimensional external flow by lattice gas methods. In R Monaco, editor, *Discrete Kinetic Theory, Lattice Gas Dynamics and Foundations of Hydrodynamics*, pages 276–285. Institute for Scientific Interchange, World Scientific, 1988.

[5] Christopher Teixeira. *Continuum Limit Of Lattice Gas Fluid Dynamics*. PhD thesis, Massachusetts Institute of Technology, Department of Nuclear Engineering, 1992. Kim Molvig Thesis Supervisor.

[6] Jeffrey Yepez. Lattice gas dynamics: Volume 1 viscous fluids. Technical report pl-tr-96-2122(i), Air Force Research Laboratory, AFRL/VSBE Hanscom AFB, MA 01731, November 1996.

[7] J.A. Somers and R.C. Rem. The construction of efficient collision tables for fluid flow computations with cellular automata. In P. Manneville, N. Boccara, G.Y. Vichniac, and R. Bidaux, editors, *Cellular Automata and Modeling of Complex Physical Systems*, pages 161–177. Springer-Verlag, Februrary 1989. Proceedings of the Winter School, Les Houches, France.

[8] Michel Hénon. Viscosity of a lattice gas. In Gary D. Doolen, editor, *Lattice Gas Methods for Partial Differential Equations*, pages 179–207. Santa Fe Institute, Addison-Wesley Publishing Company, 1990.

[9] Daniel H. Rothman. Negative-viscosity lattice gases. *Journal of Statistical Physics*, 56(3/4):517–524, 1989.

[10] Cécile Appert and Stéphane Zaleski. Lattice gas with a liquid-gas transition. *Physical Review Letters*, 64:1–4, 1990.

[11] Cécile Appert, Daniel Rothman, and Stéphane Zaleski. A liquid-gas model on a lattice. In Gary D. Doolen, editor, *Lattice Gas Methods: Theory, Applications, and Hardware*, pages 85–96. Special Issues of Physica D, MIT/North Holland, 1991.

[12] Cécile Appert and Stéphane Zaleski. Dynamical liquid-gas phase transition. *Journal de Physique II*, 3:309–337, 1993.

[13] Daniel H. Rothman and Stéphane Zaleski. Lattice-gas models of phase separation: interfaces, phase transitions, and multiphase flow. *Reviews of Modern Physics*, 1994.

[14] Jeffrey Yepez. A lattice-gas with long-range interactions coupled to a heat bath. *American Mathematical Society*, 6:261–274, 1996. Fields Institute Communications; Presented at the 1993 Lattice-Gas Conference held in Waterloo, Canada.

[15] Jeffrey Yepez. Long-range lattice-gas simulation on the cam-8 prototype. Technical report pl-tr-95-2132, Phillips Laboratory, PL/GPA Hanscom AFB, MA 01731, September 1995.

[16] Jeffrey Yepez. Lattice-gas crystallization. *Journal of Statistical Physics*, 81(1/2):255–294, 1994.

[17] J. Hardy, O. de Pazzis, and Y. Pomeau. Molecular dynamics of a classical lattice gas: Transport properties and time correlation functions. *Physical Review A*, 13(5):1949–1961, 1976.

[18] Leo P. Kadanoff, Guy R. McNamara, and Gianluigi Zanetti. A poiseuille viscometer for lattice gas automata. *Complex Systems*, 1:709–803, 1987.

[19] Leo P. Kadanoff, Guy R. McNamara, and Gianluigi Zanetti. From automata to fluid flow: Comparisons of simulation and theory. *Physical Review A*, 40(8):4527–4541, 1989.

[20] Leo P. Kadanoff, Guy R. McNamara, and Gianluigi Zanetti. A poiseuille viscometer for lattice gas automata. In Gary D. Doolen, editor, *Lattice Gas Methods for Partial Differential Equations*, pages 385–397. Santa Fe Institute, Addison-Wesley Publishing Company, 1990.

[21] Gianluigi Zanetti. Hydrodynamics of lattice-gas automata. *Physical Review A*, 40(3):1539–1548, 1989.

[22] Chris Adler, Bruce.M. Boghosian, Eric G. Flekkoy, and Daniel H. Rothman Norman H. Margolus. Simulating three-dimensional hydrodynamics on a cellular automata machine. *Journal of Statistical Physics*, 81(1/2), 1995.

[23] Bruce M. Boghosian. Correlations and renormalization in lattice gases. *Physical Review E*, 52(1), July 1995. comp-gas/9403003.

[24] Bruce M. Boghosian, Peter V. Coveney, and Andrew N. Emerton. A lattice-gas model of microemulsions. *Proceedings of the Royal Society*, A(452):1221–1250, 1996.

[25] Andrew N. Emerton, Peter V. Coveney, and Bruce M. Boghosian. Lattice-gas simulations of domain growth, saturation, and self-assembly in immiscible fluids and microemulsions. *Physical Review E*, 56(1):1286, 1997.

[26] Jean Pierre Boon. Statistical mechanics and hydrodynamics of lattice gas automata: An overview. *Physica*, D(47):3–8, 1991.

[27] P. Grosfils, J.P. Boon, and P. Lallemand. 19-bit thermal lattice-gas automaton. *Journal of Statistical Physics*, 1993.

[28] M.H. Ernst and Shankar P. Das. Thermal cellular automata fluids. *Journal of Statistical Physics*, 66(1/2):465–483, 1992.

[29] R. Brito and M.H. Ernst. Ring kinetic theory for tagged-particle problems in lattice gases. *Physical Review A*, 46(2):875–887, 1992.

[30] S.P. Das, H.J. Bussemaker, and M.H. Ernst. Generalized hydrodynamics and dispersion relations in lattice gases. *Physical Review E*, 48(1):245–255, 1993.

[31] A.J.H. Ossendrijver, A. Santos, and M.H. Ernst. Lattice gases with static disorder: Renormalization of mean field theory. *Journal of Statistical Physics*, 71(5/6):1015–1042, 1993.

[32] Michel Hénon. Implementation of the fchc lattice gas model on the connection machine. *Journal of Statistical Physics*, 68(3/4):353–377, 1992.

[33] Jill P. Dahlburg, David Montgomery, and Gary D. Doolen. Noise and compressibility in lattice-gas fluids. *Physical Review A*, 36(5):2471–2474, 1987.

[34] Hudong Chen, Shiyi Chen, Gary D. Doolen, Y.C. Lee, and H.A. Rose. Multithermodynamic phase lattice-gas automata incorporating interparticle potentials. *Physical Review A*, 40(5):2850–2853, 1989. Rapid Communications.

[35] S. Chen, G.D. Doolen, K. Eggert, D. Grunau, and E.Y. Loh. Lattice gas simulations of one and two-phase fluid flows using the connection machine-2. In A.S. Alves, editor, *Discrete Models of Fluid Dynamics*, pages 232–248. World Scientific, September 1990. Series on Advances in Mathematics for Applied Sciences, Vol. 2.

[36] Shiyi Chen, Karen Diemer, Gary D. Doolen, and Kenneth Eggert. Lattice gas automata for flow through porous media. In Gary D. Doolen, editor, *Lattice Gas Methods: Theory, Applications, and Hardware*, pages 72–84. Special Issues of Physica D, MIT/North Holland, 1991.

[37] S. Chen, G.D. Doolen, K. Eggert, D. Grunau, and E.Y. Loh. Local lattice-gas model for immiscible fluids. *Physical Review A*, 43(12):7053–7056, 1991.

[38] Shiyi Chen, Hudong Chen, Gary D. Doolen, Semion Gutman, and Minxu Lee. A lattice gas model for thermohydrodynamics. *Journal of Statistical Physics*, 62(5/6):1121–1151, 1991.

[39] Bruce M. Boghosian, Jeffrey Yepez, Francis J. Alexander, and Norman H. Margolus. Integer lattice gas. *Physical Review E*, 55(4):4137–4147, 1997. comp-gas/9602001.

[40] Bruce M. Boghosian, Jeffrey Yepez, Peter Coveney, and Alexander Wagner. Entropic lattice boltzmann methods. *Journal of Statistical Physics*, 1999. In preparation.

[41] Bruce M. Boghosian. Lattice gases illustrate the power of cellular automata in physics. *Computers in Physics*, 5(6), Nov/Dec 1991.

[42] A.W. Burks. *Essays on Cellular Automata*. University of Illinois Press, 1970.

[43] Edward Fredkin and Tommaso Toffoli. Conservative logic. *International Journal of Theoretical Physics*, 21(3/4):219–253, 1982.

[44] Stephen Wolfram. Statistical mechanics of cellular automata. *Reviews of Modern Physics*, 55(3):601–644, 1983.

[45] Stephen Wolfram. Universality and complexity in cellular automata. *Physica*, 10D:1–35, 1984.

[46] Tommaso Toffoli and Norman Margolus. *Cellular Automata Machines*. MIT Press Series in Scientific Computation. The MIT Press, 1987.

[47] Tommaso Toffoli. Computation and construction universality of reversible cellular automata. *Journal of Computer and System Sciences*, 15(2):213–231, 1977.

[48] Norman Margolus. Physics-like models of computation. *Physica*, 10D:81–95, 1984.

[49] Tommaso Toffoli. Cam: A high-performance cellular-automaton machine. *Physica*, 10D:195–204, 1984. A demonstration TM-gas experiment was part of the CAMForth software distribution.

[50] Gerard Y. Vichniac. Simulating physics with cellular automata. *Physica*, 10D:96–116, 1984.

[51] Norman H. Packard and Stephen Wolfram. Two-dimensional cellular automata. *Journal of Statistical Physics*, 38(5/6):901–946, 1985.

[52] Stephen Wolfram and James B. Salem. Thermodynamics and hydrodynamics with cellular automata. In Stephen Wolfram, editor, *Theory and Applications of Cellular Automata*, pages 362–365. World Scientific, 1986. Submitted November 1985.

[53] W. Daniel Hillis. The connection machine. *Scientific American*, 256:108–115, 1987.

[54] Tommaso Toffoli. Cellular automata as an alternative to (rather than an approximation of) differential equations in modeling physics. *Physica*, 10D:117–127, 1984.

[55] Norman Margolus, Tommaso Toffoli, and Gérand Vichniac. Cellular-automata supercomputers for fluid-dynamics modeling. *Physical Review Letters*, 56(16):1694–1696, 1986.

[56] J.P. Rivet and U. Frisch. Lattice gas automata in the boltzmann approximation. *Comptes Rendus*, 302(II):p. 267, 1986. In French. Translation appears in Lattice Gas Methods for Partial Differential Equations, SFI SISOC, Eds. Doolen et al., Addison-Wesley Publishing Co., 1990.

[57] Guy R. McNamara and Gianluigi Zanetti. Use of the boltzmann equation to simulate lattice-gas automata. *Physical Review Letters*, 61(20):2332–2335, 1988.

[58] P.L. Bhatnager, E.P. Gross, and M. Krook. A model for collision processes in gases. i. small amplitude processes in charged and neutral one-component systems. *Physical Review*, 94(3):511–525, 1954.

[59] Hudong Chen, Shiyi Chen, and William H. Mattaeus. Recovery of the navier-stokes equations using a lattice-gas boltzmann method. *Physical Review A*, 45(8):R5339–R5342, 1992.

[60] Frank J. Alexander, Hudong Chen, Shiyi Chen, and Gary D. Doolean. Lattice boltzmann model for compressible fluids. *Physical Review A*, 46(4):1967–1970, 1992.

[61] Frank J. Alexander, Shiyi Chen, and J.D. Sterling. Lattice boltzmann thermohydrodynamics. *Physical Review E*, 47(4):R2249–R2252, 1993.

[62] George Em Karniadakis and Steven A. Orszag. Nodes, modes and flow codes. *Physics Today*, 46(3):34–42, 1993.

[63] Danial O. Martinez, William H. Matthaeus, Shiyi Chen, and Dave Montgomery. Comparison of spectral method and lattice bolzmann simulations of two-dimensional hydrodynamics. *Physics of Fluids*, 6(3):1285–1298, 1994.

[64] Xiaowen Shan and Hudong Chen. Lattice boltzmann model for simulating flows with multiple phases and components. *Physical Review E*, 47(3):1815–1819, 1993.

[65] Xiaowen Shan and Hudong Chen. Simulation of nonideal gases and liquid-gas phase transitions by the lattice boltzmann equation. *Physical Review E*, 49(4):2941–2948, 1994.

[66] Xiaowen Shan and Gary Doolen. Multi-component lattice-boltzmann model with interparticle interaction. *Journal of Statistical Physics*, 81:379, 1995.

[67] Xiaowen Shan. Simulation of rayleigh-benard convection using lattice boltzmann method. *Physical Review E*, 55(3):2780–2788, 1997. Presented in 1996 at Sixth International Conference on Discrete Fluid Mechanics, Boston University, Massachusetts.

[68] Daryl Grunau, Shiyi Chen, and Kenneth Eggert. A lattice boltzmann model for multiphase fluid flows. *Physics of Fluids A*, 5(10):2557–2562, 1993.

[69] W.R. Osborn, E. Orlandini, M.R. Swift, J.M. Yeomans, and J.R. Banavar. Lattice boltzmann study of hydrodynamics spinodoidal decomposition. *Physical Review Letters*, 75(22):4031–4034, 1995.

[70] M.R. Swift, E. Orlandini, W.R. Osborn, and J.M. Yeomans. Lattice boltzmann simulations of liquid-gas and binary-fluid systems. *Physical Review E*, 54(5):5041–5052, 1996.

[71] Alexander J. Wagner and Julia M. Yeomans. Spinoidal decomposition in two-dimensional binary fluids. *International Journal of Modern Physics C*, 9(8):1373–1382, 1998.

[72] Andrew K. Gustensen and Daniel H. Rothman. A lattice-gas model for three immiscible fluids. *Physica*, D(47):47–52, 1991.

[73] Andrew K. Gustensen and Daniel H. Rothman. A galilean-invariant immiscible lattice gas. *Physica*, D(47):53–63, 1991.

[74] D. Dab and Anna Lawniczak. Cellular automaton model for reactive systems. *Physical Review Letters*, 64:2462–2465, 1990.

[75] Anna Lawniczak, D. Dab, and Ray Kapral. Reactive lattice-gas automata. *Physica D*, 47:132–138, 1991.

[76] Ray Kapral, Anna Lawniczak, and P. Masiar. Oscillations and waves in a reactive lattice-gas automaton. *Physical Review Letters*, 66:2539–2542, 1991.

[77] Hudong Chen and William H. Mattaeus. New cellular automaton model for magnetohydrodynamics. *Physical Review Letters*, 58(18):1845–1848, 1987.

[78] Hudong Chen and William H. Mattaeus. An analytic theory and formulation of a local magnetohydrodynamic lattice gas model. *Physics of Fluids*, 31(6):1439–1455, 1988.

[79] Shiyi Chen, Hudong Chen, Daniel Martínez, and William Matthaeus. Lattice boltzmann model for simulation of magnetohydrodynamics. *Physical Review Letters*, 67(27):3776–3779, 1991.

[80] Danial O. Martinez, Shiyi Chen, and William H. Matthaeus. Lattice boltzmann magnetohydrodynamics. *Physics of Plasmas*, 1(6):1850–1867, 1994.

[81] Daniel Rothman. Macroscopic laws for immiscible two-phase flow in porous media: results from numerical experiments. *Journal of Geophysical Research*, 95:8663, 1990.

[82] T.R. Kirkpatrick and M.H. Ernst. Kinetic theory for lattice-gas cellular automata. *Physical Review A*, 44(12):8051–8061, 1991.

[83] R. Brito and M.H. Ernst. Lattice gases in slab geometries. *Physical Review A*, 44(12):8384–8687, 1991.

[84] Washington Taylor IV and Bruce M. Boghosian. Renormalization of lattice gas transport coefficents. Technical Report Series TMC-208, Thinking Machines Corportation, September 1991. Also presented by Boghosian at the Internation Conference on Pattern Formation and Lattice-Gas Automata, June 1993.

[85] R. Brito and M.H. Ernst. Ring kinetic theory for tagged-particle problems in lattice gases. *Physical Review A*, 46(2):875–887, 1992.

[86] René van Roij. Ring kinetic theory of the boghosian-levermore cellular automaton. Master's thesis, Institute for Theoretical Physics University of Utrecht, August 1992. Supervisor: Prof M.H. Ernst.

[87] A.J.H. Ossendrijver, A. Santos, and M.H. Ernst. Lattice gases with static disorder: Renormalization of mean field theory. *Journal of Statistical Physics*, 71(5/6):1015–1042, 1993.

[88] Bruce M. Boghosian. Correlations and renormalization in lattice gases. *Physical Review E*, 52(1), 1995. comp-gas/9403003.

[89] B.J. Alder and T.E. Wainwright. Velocity autocorrelations for hard spheres. *Physical Review Letters*, 18(23):988–990, 1967.

[90] Yves Pomeau. A new kinetic theory for a dense classical gas. *Physics Letters*, 27A(9):601–602, 1968.

[91] M.H. Ernst, E.H. Hauge, and J.M.M van Leeuwen. Asymptotic time behavior of correlation functions. *Physical Review Letters*, 25(18):1254–1256, 1970.

[92] Ray Kapral and Anna Lawniczak. Bibliography for special 1994 lattice gas issue of the fields institute series. In Ray Kapral and Anna Lawniczak, editors, *Proceedings of the Pattern Formation and Lattice-Gas Automata NATO Advanced Research Workshop*. Fields Institute for Research in Mathematical Sciences, American Mathematical Society, 1993.

[93] Leo P. Kadanoff and Jack Swift. Transport coefficients near the critical point: A master-equation approach. *Physical Review*, 165(1):310–322, 1967.

[94] A. Lamura, G. Gonnela, and Julia M. Yeomans. Modeling the dynamics of amphiphilic fluids. *International Journal of Modern Physics C*, 9(8):1469–1478, 1998.

[95] Steven A. Orszag and Victor Yakhot. Reynolds number scaling of cellular-automaton hydrodynamics. *Physical Review Letters*, 56(16):1691–1693, 1986.

[96] L.D. Landau and E.M. Lifshitz. *Fluid Mechanics*, volume 6 of *Course of Theoretical Physics*. Pergamon Press, 2nd edition, 1987.

[97] P.M. Binder. The properties of tagged lattice fluids: I: Diffusion coefficients. In R Monaco, editor, *Discrete Kinetic Theory, Lattice Gas Dynamics and Foundations of Hydrodynamics*, pages 28–37. Institute for Scientific Interchange, World Scientific, 1988.

[98] Patrick Grosfils, Jean-Pierre Boon, Ricardo Brito, and Matthieu H. Ernst. Statistical hydrodynamics of lattice-gas automata. *Physical Review E*, 48(4):2655–2668, 1993.

[99] H.J. Bussemaker, M.H. Ernst, and J.W. Duffy. Generalized boltzmann equation for lattice gas automata. *Journal of Statistical Physics*, 78(5/6):1521–1554, 1995.

[100] Jeffrey Yepez. Lattice-gas quantum computation. *International Journal of Modern Physics C*, 9(8):1587–1596, 1998. Proceeding of the 7th International Conference on the Discrete Simulation of Fluids, University of Oxford.

[101] Jeffrey Yepez. Quantum computation of fluid dynamics. In Collin P. Williams, editor, *Quantum Computing and Quantum Communications*, page 480pp. Lecture Notes in Computer Science, Springer-Verlag, 1999. First NASA International Conference, QCQC'98, Palm Springs, California, USA, February 17-20, 1998, Selected Papers.

[102] B. Dubrulle, U. Frisch, M. Hénon, and J.P. Rivet. Low-viscosity lattice gases. *Physica*, D(47):27–29, 1991.

[103] Yue Hong Qian. *Gaz sur Réseaux et Théorie Cinétique sur Réseaux Appliquée à l'Equation de Navier-Stokes*. PhD thesis, Universite De Paris, L'Ecole Normale Superieure, Departement De Physique, 1990.

[104] Jeffrey Yepez, Guy P. Seeley, and George Mou. Lattice-gas automata on parallel architectures. In *Proceedings of International Symposium on Parallel Computation*, pages 522–525, 1993. Beijing, China.

[105] Tommaso Toffoli. Fine-grained parallel supercomputer. Technical report pl-tr-95-2013, Phillips Laboratory, Contract No. F196828-94-C-0068 Step Research 26 Athens Street, Cambridge, MA 02138, November 1994.